



Enhancement of off-body communications with a low-SAR, high-gain multiband patch antenna designed with a quad-band artificial magnetic conductor

Vellaichamy Rajavel  and Dibyendu Ghoshal

Department of ECE, National Institute of Technology Agartala, Agartala, Tripura, India

Research Paper

Cite this article: Rajavel V, Ghoshal D (2024) Enhancement of off-body communications with a low-SAR, high-gain multiband patch antenna designed with a quad-band artificial magnetic conductor. *International Journal of Microwave and Wireless Technologies* **16**(2), 318–338. <https://doi.org/10.1017/S1759078723001174>

Received: 15 February 2023
Revised: 27 September 2023
Accepted: 03 October 2023

Keywords:

artificial magnetic conductor; front-to-back ratio; high gain; low specific absorption rate; multiband antenna

Corresponding author: V. Rajavel;
Email: rajavel572@gmail.com

Abstract

The increasing demand for wireless communication has emphasized the need for multiband antennas. This study presents a novel design for a multiband antenna with reduced specific absorption rate (SAR), high gain, and improved front-to-back ratio (FBR) achieved through the integration with a 4×4 artificial magnetic conductor (AMC) surface. The proposed antenna covers a wide range of wireless frequency bands, including Industrial, Scientific, and Medical, Wireless Local Area Network, Worldwide Interoperability for Microwave Access, Wi-Fi 6E, and 7, with resonating frequencies at 2.4, 3.2, 5.5, 7.5, and 10 GHz. The AMC unit cell creates four zero-degree reflection phases with double negative properties at 2.5, 3.8, 5.5, and 7.5 GHz. The compact design measures $0.23\lambda_0 \times 0.296\lambda_0 \times 0.0128\lambda_0$ and placed $0.104\lambda_0$ above an AMC surface of size $0.512\lambda_0 \times 0.512\lambda_0 \times 0.1296\lambda_0$. This structure enhances the gain by up to 8.55dBi at 6.01 GHz. The proposed antenna has -10 dB impedance bandwidth for these corresponding frequencies viz 2.34–2.43 GHz (3.77%), 2.81–3.83 GHz (30.72%), 4.82–6.21 GHz (25.20%), 7–7.65 GHz (8.87%), and 8.06–10.31 GHz (24.5%). An overall average percentage reduction value of SAR taken at these frequencies has been found to be 96.11% with AMC structure. The antenna sample was successfully fabricated, and the experimental results have been found to match well with the simulation results. This integrated design offers a promising solution for wearable off-body communication devices.

Introduction

The growth in new wireless services and the emergence of novel technology uses will propel the development of advanced wireless communication systems that can effectively and efficiently handle various tasks. The wireless body area network (WBAN) has recently garnered significant attention in academic research for its potential to revolutionize wireless communication technologies. The health-care industry, military and emergency rescue operations, sports, and other sectors are expected to be significant adopters of WBAN due to its low-cost and high-quality wireless network services. The communication links in WBAN rely on multiband antennas to perform various functions [1]. Hence, multiband, low-profile, high-gain antennas will be essential for WBAN and the upcoming 6G networks. The design of microstrip antennas has shifted toward structural simplification, which is becoming a key trend while still maintaining the desired features of multiband capability, impedance bandwidth, realized gain, and outstanding performance. The mortality rates related to COVID-19 continue to increase worldwide, particularly among the elderly and individuals with pre-existing medical conditions. Health-care professionals must exercise additional caution while treating patients with COVID-19 due to the contagious nature of the virus, making it imperative to adopt a non-invasive approach. WBAN communication, specifically wearable technology, has emerged as a promising solution. Researchers are currently focusing on the antennas utilized in WBAN communication, as they play a crucial role in its success. Microstrip patch antennas, with their versatility and efficiency, have been a popular choice for wireless communication systems for the past three decades. Their use in the medical field has recently seen tremendous growth due to their numerous advantages.

Wearable electronics require compact, flexible antennas and offer high gain while ensuring low specific absorption rate (SAR) levels. In addition, a WBAN allows data transmission between nearby wearables (known as “on-body communication”) or to wearables that are more distant (referred to as “off-body communication”). Antennas embedded in or wrapped around the user enable these communications. When designing WBAN antennas, factors such as SAR and polarization mismatch must be considered, making the design process distinct from conventional antennas. Antennas used in WBAN applications, particularly for off-body communication, must be able to transmit signals across several frequency bands in specific directions. A single antenna configuration may be necessary to meet the demands of

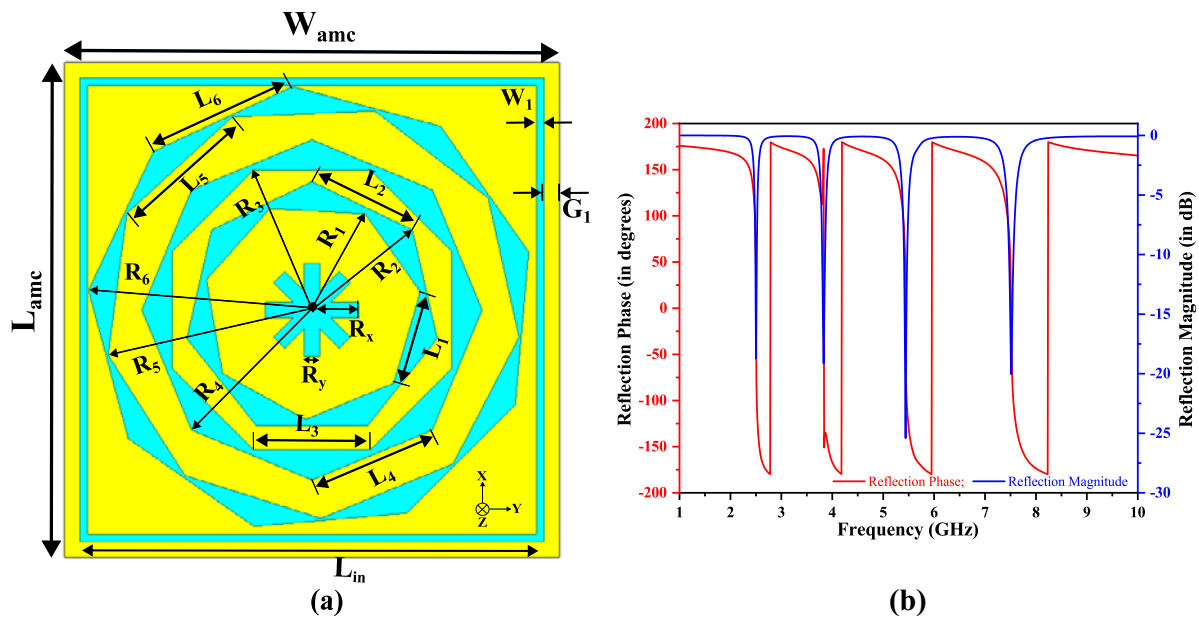


Figure 1. The design and response of the proposed unit cell (a) geometry and (b) reflection phase and magnitude.

multiband communication. Methods for creating multiband antennas include radiation patch slots and fractal technology [2]. The radiation performance of these antennas can be improved through artificial magnetic conductor (AMC), which has in-phase reflections and can be considered as a super material. AMC produces a plane-wave reflection with the same electromagnetic characteristics as the incident wave, leading to a low-profile design with a unidirectional radiation pattern, superior performance, and low back radiation.

A wide range of advanced techniques and models have been proposed recently for designing antennas and AMCs [3–7]. Different shaped and sized antennas, such as wearable antennas [8], planer inverted-F antennas [9], microstrip antennas [10, 11], monopole antennas [12], and AMC-supported multiple-input multiple-output (MIMO) antennas [13], have been suggested for WBAN communications. However, these antennas are limited to a single frequency range, making multilink transmission impossible. In paper [14], an AMC reflector-backed dual-band, dual-polarized antenna of $70.4 \times 76.1 \times 43.11 \text{ mm}^3$ size was designed for Wireless Local Area Network (WLAN) usage. It showed a zero-degree reflection coefficient at two resonance frequencies with strong gain enhancement performance. Yang et al. [15] proposed a dual-band patch antenna with separate radiating elements to achieve different radiation properties, with a maximum gain of 3.1 dBi at the lower frequency. The antennas in papers [16] and [17] have gains more significant than 10 dB, but their complex structures and large size hinder their application. Thus, the challenge remains to develop a compact, wideband microstrip antenna with high gain, high efficiency, low cost, and lightweight. Yang et al. [18] presented a dual-band antenna that is flexible and capable of dual circular polarization, high gain, and low backward radiation, making it suitable for long-range connections. Antenna operating in the 5.8 GHz Industrial, Scientific, and Medical (ISM) and 3.5 GHz Worldwide Interoperability for Microwave Access (WiMAX) bands are designed for wearable devices. Annavarapu et al. [19] developed a planar antenna based on dielectric AMC for Internet of Things applications in the P band, with a small

Table 1. Summary of optimized AMC unit cell parameters

Parameters	Value (mm)	Parameters	Value (mm)	Parameters	Value (mm)
W_{ams} & L_{ams}	16	L_4	4.25	R_6	7.25
G_1	1	L_5	4.6	R_x	1.5
L_{in}	15	L_6	5	$R_y, W_2, \& W_1$	0.5
L_1	3.1	R_1	3.55	$W_3 \& W_4$	0.6
L_2	3.6	R_2	4.15	R_4	5.5
L_3	3.75	R_3	4.9	R_5	6.75

patch size of $0.16\lambda_0 \times 0.20\lambda_0 \times 0.01 \lambda_0$ and a gain of 3.1 dBi. Gupta et al. [20] showed a fractal H-shaped antenna with a flawed ground structure, with circular polarization that makes it suitable for use with Bluetooth, LTE, GNSS, S-, and C-band devices.

The previous studies in the field mainly concentrated on improving the performance of single- or dual-band antennas by incorporating AMCs with limited frequency coverage. A triband microstrip antenna with a tricyclic stacked structure was proposed in paper [21], featuring good gain across three frequency ranges and an elliptic-shaped defected ground structure to enhance bandwidth and radiation efficiency. Another research [22] explored a patch antenna that met the criteria of being triband, had improved bandwidth, high gain, and a diverse radiation pattern, with a gain of 6.35 dBi at 1.79–1.81 GHz, 6.1 5dBi at 3.74–4.0 GHz, and 9.42 dBi at 4.93–5.44 GHz. However, designing triband AMC-backed antennas is challenging since it requires a complex design of an AMC with three or more zero-degree phases in its reflection coefficient, and few triband AMC-based antennas have been reported so far. Despite these challenges, researchers have been making significant efforts to develop AMC-supported multiband antennas.

The use of AMCs in microstrip antennas has been well documented in the literature to enhance the radiation performance of

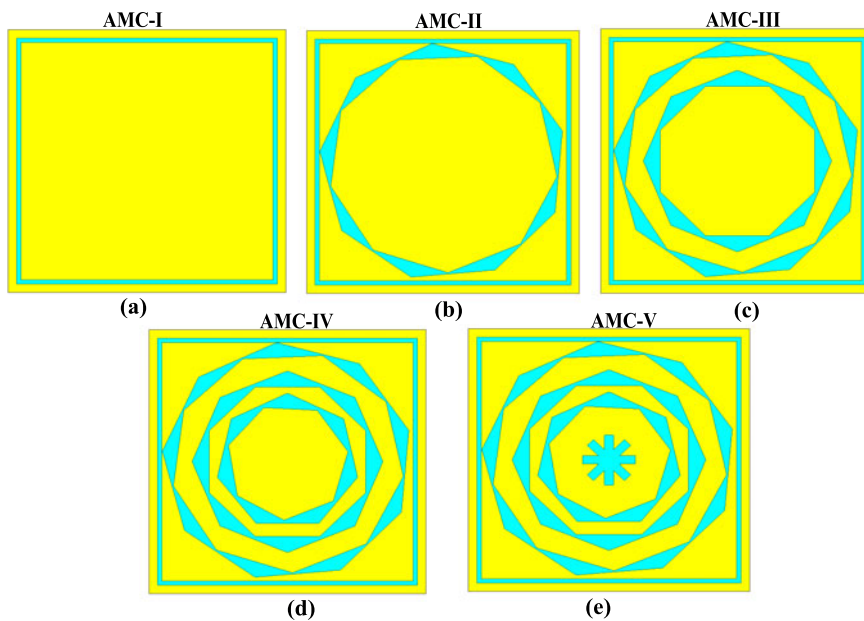


Figure 2. The evolution of the AMC unit cell: (a) AMC-I, (b) AMC-II, (c) AMC-III, (d) AMC-IV, and (e) AMC-V.

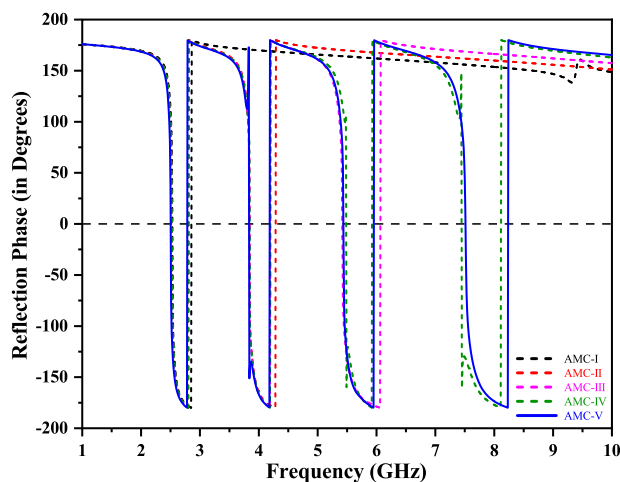


Figure 3. The reflection phase response of the AMC unit cell at various evolutionary stages.

the antenna. In paper [23], a slotted dipole antenna with a compact profile and a broad operating frequency range is presented, utilizing an AMC structure of 6×6 unit cells. This design achieved gains of up to 9.9 dB in the C band. In paper [24], a blueprint is developed for a bilayer AMC, where the dipole and patch hybrid modes are activated using a single feeding and standard aperture, resulting in an impressive 51.3% impedance bandwidth across the frequency range of 1.68–2.8 GHz. The ultra-wideband meta surface reported in paper [25] can switch from linear to circular polarization with over 93% efficiency, covering a frequency span from 7.08 to 25.86 GHz. Reflector elements have been proposed for construction on a reconfigurable AMC platform, with a return loss of -15 dB and 12 different radiation patterns, as described in paper [26]. El Atrash et al. [27] explain the CRLH (composite right/left-handed) approach to the π -section and the strategic installation of a 2×2 AMC array for better performance in WBAN and medical settings. Saeed et al. [28] report a new flexible and reconfigurable antenna for mobile remote patient monitoring systems,

emitting orthogonally polarized waves in the WBAN and WiMAX spectrum and a polarization-dependent dual-band AMC surface to enhance radiation performance and reduce SAR. In paper [29], a quad-band coplanar waveguide antenna equipped with an AMC, including four zero-phases of the reflection coefficient, is used to achieve multiband and high-gain features. The present paper aims at to design a novel multiband AMC-based antenna by overcoming the aforementioned limitations.

This paper outlines a novel design for a low-profile, high-gain, low-SAR multiband AMC patch antenna for off-body communication systems. The design incorporates a polygonal radiating patch with different segment counts and an AMC surface of 4×4 unit cells placed at a distance of $0.104\lambda_0$ from the bottom of the antenna. The polygonal patch is constructed with three patches of varying segment counts that are rotated concerning each other to provide multiband responses. The AMC unit cell generates four zero-degree reflection phase responses with double negative (DNG) behavior at 2.5, 3.8, 5.5, and 7.5 GHz. The proposed patch antenna and AMC surface combination generate five distinct resonance points at 2.4, 3.2, 5.5, 7.5, and 10 GHz. The antenna reaches its highest gain at 6.01 GHz, reaching 8.55 dBi, and boasts an impressive 31.5 dB front-to-back ratio (FBR) at 4.5 GHz. The proposed antenna has dimensions of $0.23\lambda_0 \times 0.296\lambda_0 \times 0.0128\lambda_0$, not including the AMC surface. Human phantom simulations have shown the combined design to have a SAR of 0.0627 W/kg at 2.4 GHz. The proposed antenna and AMC surface were tested and verified in a vector network analyzer (VNA) and an anechoic chamber.

Design and characterization of a quad-band AMC unit cell

Design and geometry of AMC unit cell

There has been significant research on thin-layer AMC structures that act as perfect magnetic conductors at the resonance frequency [30]. The 4×4 AMC surface is constructed by arranging periodic unit cells with a gap of 0.1 mm (G_g). The unit cell comprises a dielectric substrate and a metallic ground. The normal incidence illumination of a plane wave is used as the standard benchmark

for evaluating the properties of an ideal AMC. The operating bandwidth of an AMC structure is defined by the phase range $[+90^\circ, -90^\circ]$, and the resonance frequency corresponds to phase 0° of the reflection coefficient. A zero-degree reflection coefficient for the AMC plane in the operating frequency range signifies that it will produce in-phase reflection concerning the incident wave. However, designing a simple structure that can reflect various zero-phase AMC frequencies in the required spectrum is challenging. The AMC is designed to provide four zero-phase reflections to enhance the radiation performance of the proposed multiband antenna.

The proposed AMC unit cell design, as depicted in Fig. 1(a), consists of a square patch and three polygonal patches with varying numbers of segments. The unit cell has a compact size of $16 \times 16 \times 1.6 \text{ mm}^3$ and is constructed using the FR4 material, which has a relative permittivity of 4.4 and a loss tangent of 0.02. The simulation of the unit cell was performed using ANSYS HFSS with the incorporation of the floquet port and master-slave boundary conditions. In Fig. 1(b), the reflection phase and magnitude response of the proposed AMC unit cell is illustrated, with zero-phase reflection observed at frequencies of 2.5, 3.8, 5.5, and 7.5 GHz. The width of the nonagon, octagon, and heptagon metal strips is represented as W_2 , W_3 , and W_4 , respectively. A summary of the unit cell's optimal parameters is provided in Table 1.

Development of the AMC unit cell

The evolution of the AMC unit cell involved five stages of development. Three fundamental components make up the final unit

cell design. These are a square-shaped patch, a polygonal patch composed of three metal segments, and an arrangement of eight rectangular patches. The entire design process is illustrated in Fig. 2, with each stage designated as AMC-I through AMC-V. The initial stage, shown in Fig. 2(a), features a conventional square patch that accommodates the wireless frequency spectrum and exhibits zero-degree reflection at 2.5 GHz. The subsequent stages, from AMC-II to AMC-IV, involve polygonal metallic patches created by drawing a circle and labeling its circumference with the desired number of segments using ANSYS HFSS. In the second stage, AMC-II, a nonagon-shaped patch was implemented, consisting of an outer and an inner nonagon with radii R_6 and R_5 , and side lengths L_6 and L_5 , respectively. The inner nonagon was rotated relative to the outer nonagon so that its corners would fall precisely in the middle of the sides of the outer nonagon. The reflection phase response of AMC-II, which exhibits a second zero-degree reflection at 3.85 GHz, is depicted in Fig. 2(b). Figure 3 presents the reflection phase response.

The development of the AMC-III and AMC-IV followed the success of Step 2. Figure 2(c) and (d) shows the AMC-III and AMC-IV, respectively, created with an octagon and heptagon shape. In Step 4, the proposed unit cell had four frequencies (2.52, 3.84, 5.48, and 7.44 GHz) identified with a zero-degree reflection phase. Although a quad-band AMC was produced, the bandwidth and material properties were not optimal, and the third- and fourth-band responses needed to be improved. Therefore, the AMC-V design in Fig. 2(e) was created by adding eight additional rectangular patches of size $R_x \times R_y$ to AMC-IV in Step 5. With these modifications, AMC-V showcased the desired DNG characteristics

Table 2. Bandwidth comparison of AMC unit cell development stages

AMC Design Step	Resonant Frequency (GHz)	First Band		Second Band		Third Band		Fourth Band	
		BW (GHz)	BW (%)	BW (GHz)	BW (%)	BW (GHz)	BW (%)	BW (GHz)	BW (%)
1	2.53	2.52–2.54	0.791	–	–	–	–	–	–
2	2.52, 3.84	2.5–2.53	0.396	3.83–3.85	0.521	–	–	–	–
3	2.52, 3.84, 5.42	2.51–2.53	0.794	3.83–3.85	0.521	5.39–5.44	0.923	–	–
4	2.52, 3.84, 5.48, 7.44	2.51–2.54	1.188	3.83–3.85	0.521	5.48–5.49	0.182	7.44–7.45	0.134
5	2.5, 3.8, 5.5, 7.5	2.48–2.52	1.6	3.79–3.82	0.788	5.51–5.59	1.441	7.46–7.55	1.199

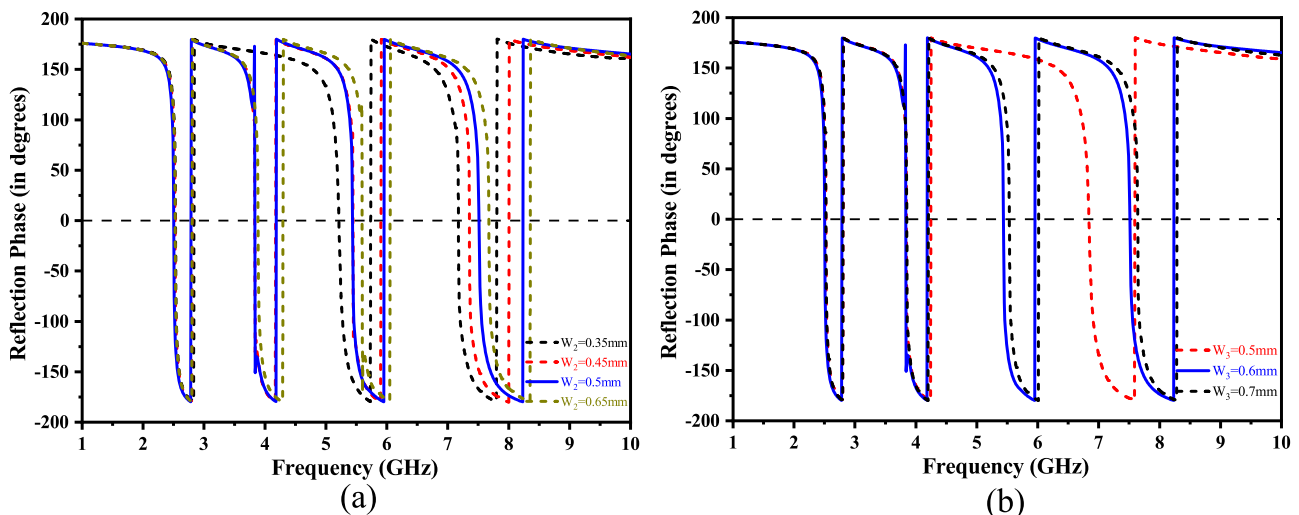


Figure 4. Parametric analysis of the unit cell: The effect of variations in (a) W_2 and (b) W_3 .

and zero-degree reflection phase at 2.5, 3.8, 5.5, and 7.5 GHz. Table 2 summarizes the bandwidth results of the AMC unit cell at each step in its evolution process.

$$\varphi = \text{Im} \left\{ \ln \left(\frac{Z_{s_AMC} - \eta}{Z_{s_AMC} + \eta} \right) \right\} \tag{1}$$

$$Z_{s_AMC} = \frac{j\omega L}{1 - \omega^2 LC} \tag{2}$$

Exploring the impact of unit cell parameters on AMC design

The resonant frequency of the AMC unit cell has been optimized by exploring two critical parameters in five different stages. First, the reflection phase of the incident wave that strikes the surface is described by equations (1) and (2) [31]. The reflection phases of the simulated quad-band AMC are depicted in Fig. 4, which varies according to the values of W_2 and W_3 . The parameter W_2 significantly influences the fourth frequency band, causing the resonant point for the fourth band to move to a higher frequency as W_2 increases.

On the other hand, W_3 affects both the third and fourth frequency bands. As a result, the AMC exhibits triband behavior only when $W_2 = 0.35$ mm and $W_3 = 0.3$ mm. The optimal parameters of the unit cell, calculated by applying equations (1) and (2) to the reflection phases of the AMC unit cell, are presented in Table 1.

AMC unit cell with different incidence angles

The dependence of the surface impedance (Z_{s_AMC}) of the AMC unit cell on the incidence angle of plane waves can be attributed to its behavior as a high impedance surface [32]. The behavior of the impedance for both transverse electric (TE) and transverse magnetic (TM) polarized waves varies based on the angle of incidence. The stability of the AMC structure against changes in the incidence angle has been studied by evaluating the phase–frequency relationship of the reflection coefficient for incident angles (θ) ranging from 0° to 180° for both TE and TM polarized waves as shown in Fig. 5. TE- and TM-polarized waves have incidence angles from 0° to 180° . Despite the change in incidence angle, the first two operational bands remain unchanged for both types of polarized waves. However, the third and fourth resonant frequencies of TE

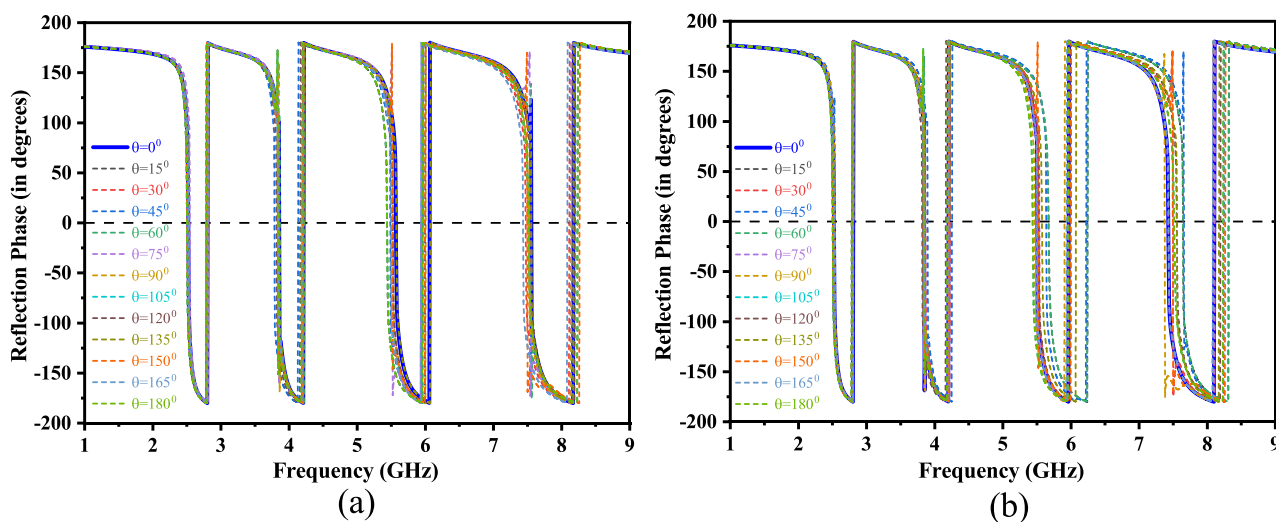


Figure 5. Reflection phase response of AMC unit cell for different incident angles: (a) TE polarization and (b) TM polarization.

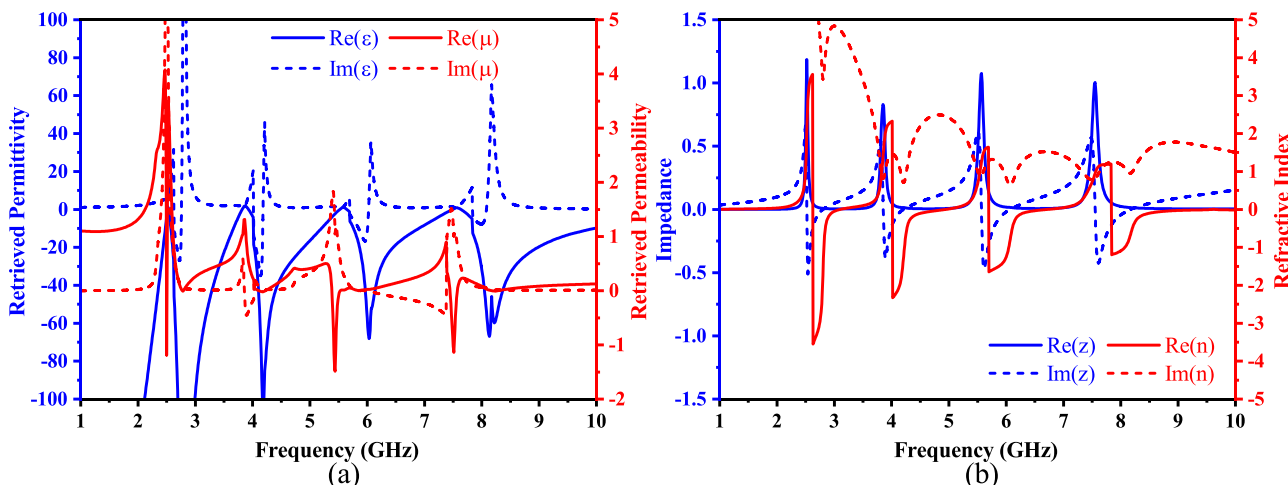


Figure 6. Characteristics of AMC unit cell: (a) Permittivity and permeability, (b) normalized impedance and refractive index.

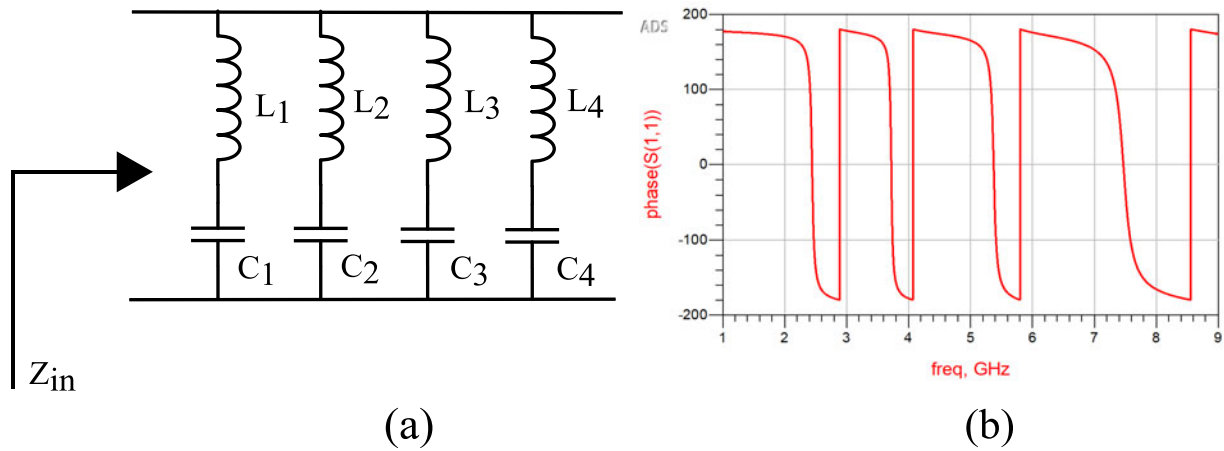


Figure 7. (a) Equivalent circuit diagram of the AMC unit cell (b) Reflection phase response of the AMC unit cell from the ADS simulator.

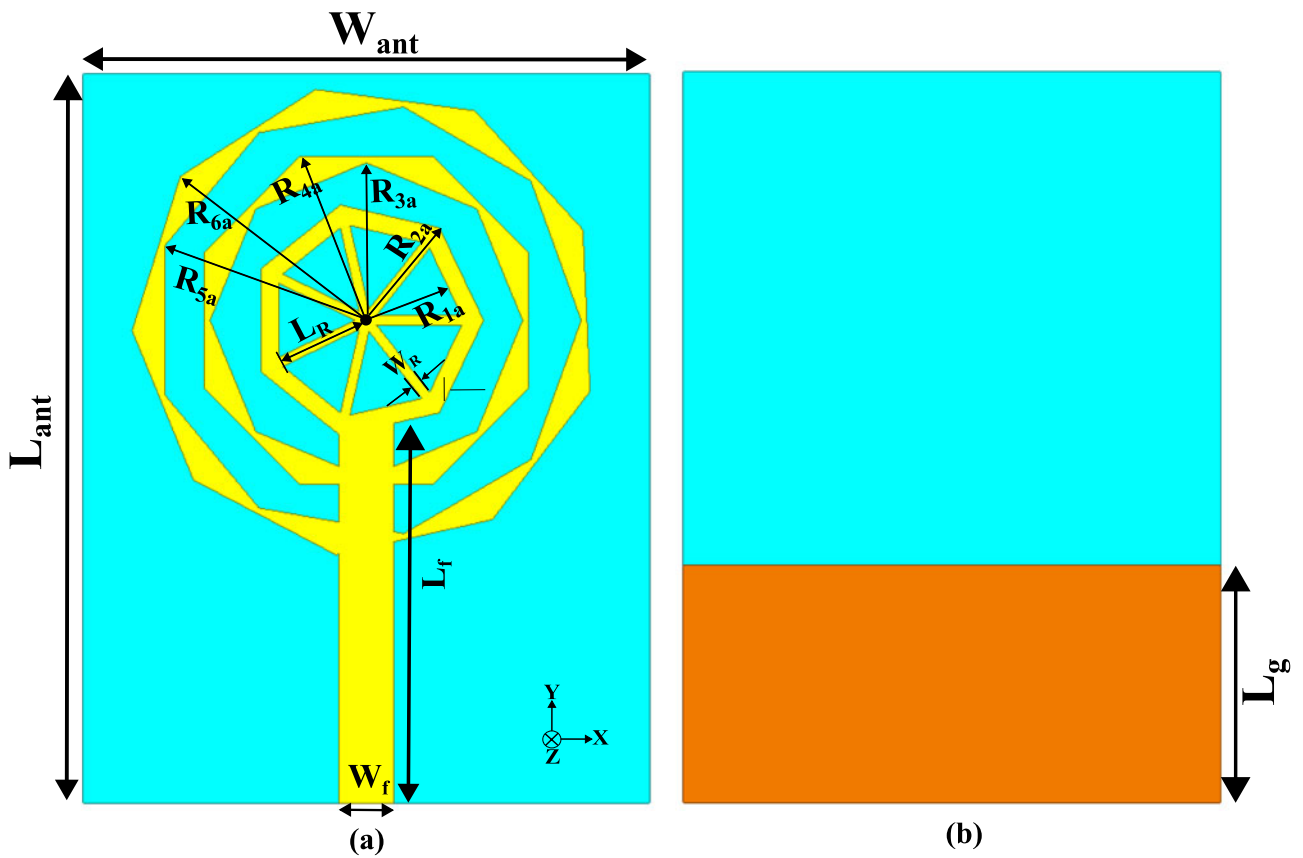


Figure 8. The geometry of the proposed antenna: (a) An overview from above and (b) a view from below.

Table 3. Optimized multiband antenna design parameters

Parameters	Value (mm)	Parameters	Value (mm)	Parameters	Value (mm)	Parameters	Value (mm)
W_{ant}	27	R_{2a}	6	R_{6a}	12	L_R & R_{1a}	5
L_{ant}	39	R_{3a}	8	W_R	0.5	R_{5a}	11
L_g	12	R_{4a}	9	W_f	2.75	L_f	19.5

polarized waves decrease to 5.3 and 7.3 GHz respectively when the incidence angle shifts from 0° to 45° or from 135° to 180°. For other

incidence angles, the resonance frequency may fluctuate, but not to a significant extent.

Table 4. Comparison of antenna designs in the evolution process

Evolution Step	Operating Frequency (GHz)	Resonant Frequency (GHz)	S_{11} (dB)	-10 dB Impedance Bandwidth (%)
1	2.62–2.77	2.72	-39.65	5.56
	3.04–5.01	3.37	-30.45	48.95
	5.48–7.20	6.27	-19.78	27.13
	7.60–8.58	8.18	-22.62	12.11
	9.55–11.4	10.97	-30.77	17.66
2	2.38–2.45	2.43	-26.42	2.89
	2.79–4.50	3.15	-42.59	46.91
	4.97–6.39	5.78	-27.37	25
	7.28–7.95	7.61	-30.66	8.79
	9.62–11.2	10.3	-34.24	15.18
3	2.36–2.44	2.41	-28.11	3.33
	2.74–4.54	3.08	-43.96	49.45
	4.99–6.37	5.72	-30.63	24.29
	7.21–7.79	7.54	-18.27	7.73
	8.78–10.64	10.04	-18.16	19.15
4	2.37–2.44	2.41	-26.4	2.91
	2.85–4.42	3.26	-46.30	43.2
	4.96–6.35	5.6	-21.75	24.6
	7.08–7.88	7.5	-28.28	10.7
	8.07–10.37	10	-16.94	24.95

The variation in bandwidth observed is only 0.05%. The resonant frequencies remained unchanged for TM polarized waves with incidence angles between 0° and 30° and 150° and 180° . However, as the incidence angle increased from 45° to 135° , there was a shift in the resonant frequency of the last two bands, with an average variance of 0.25% in bandwidth observed. The angular stability of the AMC highlights the polarization independence of isotropic unit cells. Thanks to the investigation of the AMC surface's reflection phase for various incident angles, the proposed AMC unit cell can function for any incidence angle of plane waves.

Investigating the material properties of the AMC unit cell

The S-parameters retrieval technique can determine electromagnetic properties, including complex permittivity and permeability, refractive index, and impedance [33]. The simulation software ANSYS HFSS, widely recognized and legally accessible, will be utilized to obtain the S-parameters. This simulator can extract the properties of the unit cell through the S-parameters. The proposed metamaterial's unit element, which has lattice vectors in three dimensions, will be considered, and the proper master-slave boundary conditions and Floquet port excitations will be applied to retrieve the necessary parameters. Once S_{11} and S_{21} have been extracted from ANSYS HFSS, refractive index and impedance can be calculated using equations (3) and (4). The permittivity and permeability of the unit cell can then be extracted from the refractive index and impedance of the material.

$$n = \frac{\lambda}{2\pi L_{\text{amc}}} \cos^{-1} \left[\frac{1}{2S_{21}} (1 - S_{11}^2 + S_{21}^2) \right] \quad (3)$$

$$z = \sqrt{\frac{(1 + S_{11}^2 - S_{21}^2)}{(1 - S_{11}^2 - S_{21}^2)}} \quad (4)$$

Negative values for the retrieved permittivity are observed in all bands apart from the second band, while negative values for the retrieved permeability are observed at every resonant frequency. Therefore, the designed unit cell element exhibits DNG behavior in the operational bands, as shown in Fig. 6(a). Figure 6(b) displays the retrieved refractive index and impedance, which indicates that the structure is well-matched at the resonant frequency, where the refractive index is negative.

AMC unit cell equivalent circuit analysis

The Advance Design System (ADS) software is utilized to model and test the equivalent circuit. The quad-band reflection phase behavior of the equivalent circuit was modeled by calculating the surface impedance of a patch unit cell with a combination of polygonal and square shapes. The resonant frequency of the unit cell was calculated using equation (5).

$$f_r = \frac{1}{2\pi\sqrt{LC}} \quad (5)$$

A standard inductor–capacitor resonator was found to describe the AMC surface unit cell, and the distribution components in Fig. 7(a) were estimated using the equations presented [34].

$$C = \frac{2\varepsilon}{\pi W_{\text{amc}}} \cosh^{-1} \left(\frac{p}{G_g} \right) \quad (6)$$

$$L = \frac{\pi W_{\text{amc}} \mu}{2 \cosh^{-1} \left(\frac{p}{G_g} \right)} \quad (7)$$

The width of an AMC unit cell (W_{amc}), its periodicity (p), and the distance between two adjacent unit cells (G_g) were used to calculate the equivalent capacitance using transmission line theory, which was based on the distribution of electric fields between adjacent sections, and the equivalent inductance, which was based on the height of the medium. The values of the lumped components are $L_1 = 0.8178$ nH, $L_2 = 0.2597$ nH, $L_3 = 0.2288$ nH, $L_4 = 0.3525$ nH, $C_1 = 5.2$ pF, $C_2 = 7.05$ pF, $C_3 = 3.835$ pF, and $C_4 = 1.289$ pF. The simulated reflection phase response from the circuit model in ADS, shown in Fig. 7(b), has a narrower bandwidth than the results obtained from HFSS, which tends to have a broader bandwidth due to the reflection phase. Despite this difference, the zero-reflection phase at the four bands is very similar to the HFSS results, indicating that the results are in good agreement.

Design and analysis of multiband antenna

Multiband antenna design configuration

The polygonal ring-shaped antenna is designed to support the commonly used wireless frequency ranges in communication devices outside the human body. The antenna supports ISM, WiMAX, WLAN, Wi-Fi 6E & 7, and C-band standards. Figure 8 illustrates the layout of the multiband patch antenna that utilizes a defective ground structure in the bottom metal plate to attain a multiband response with broad impedance bandwidth.

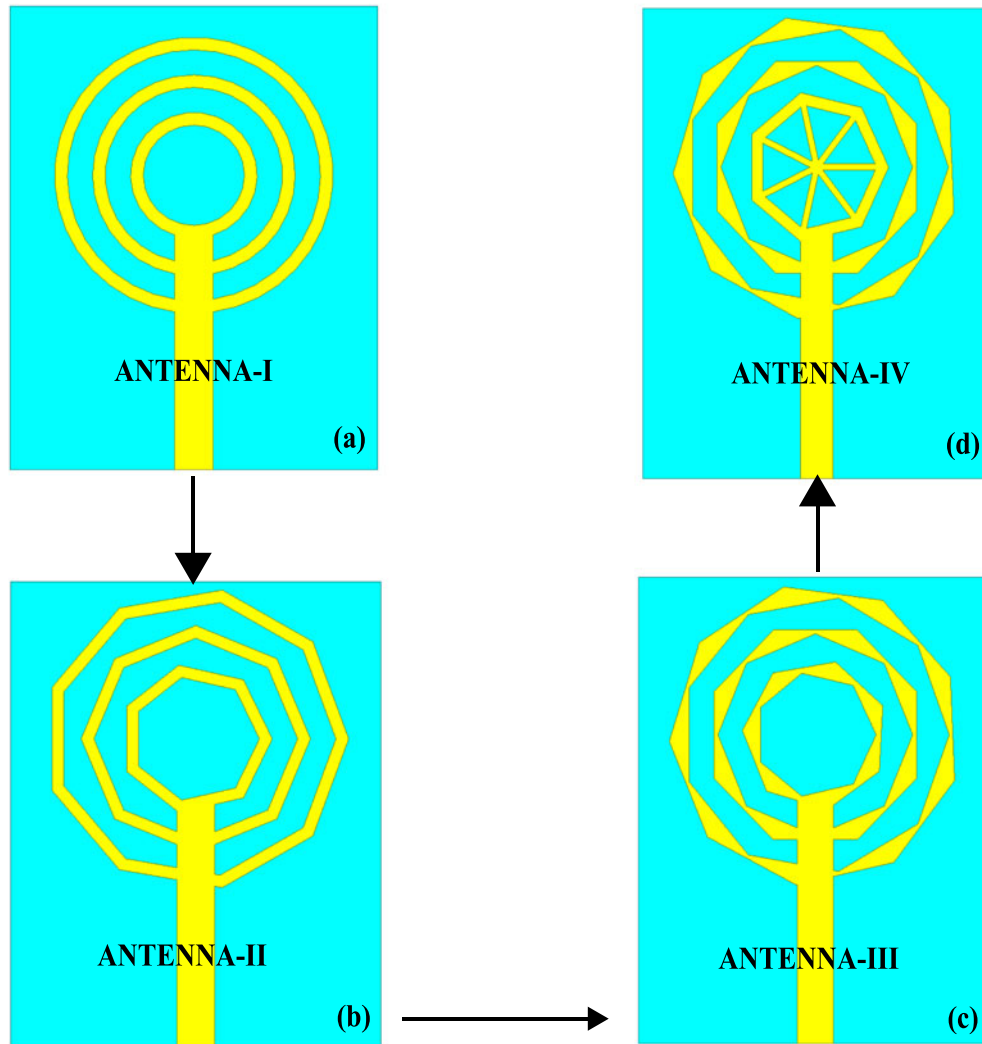


Figure 9. Development stages of the multiband antenna: (a) Antenna-I, (b) Antenna-II, (c) Antenna-III, and (d) Antenna-IV.

The patch comprises multiple polygonal rings with varying segment lengths positioned above the 1.6-mm thick FR4 substrate with a relative permittivity of 4.4 and a loss tangent of 0.02. The front and back views of the antenna are shown in Fig. 8(a) and (b), respectively, with dimensions of $29 \times 37 \times 1.6 \text{ mm}^3$. The antenna is fed by a signal through a microstrip line, resulting in an impedance bandwidth of 2.91% (2.37–2.44 GHz), 43.2% (2.85–4.42 GHz), 24.6% (4.96–6.35 GHz), 10.7% (7.08–7.88 GHz) and 24.95% (8.07–10.37 GHz). The geometrical parameters of the antenna design were optimized using ANSYS HFSS, and the results are displayed in Table 3.

Development of the multiband antenna

The comparison of the antennas developed during the evolution process is presented in Table 4 to provide a clearer understanding of the process and how the proposed antenna operates. The proposed multiband antenna consists of metal patches in polygon shapes, which have undergone a four-step transformation, as depicted in Fig. 9. The antenna resonates at 2.4, 3.2, 5.5, 7.5, and

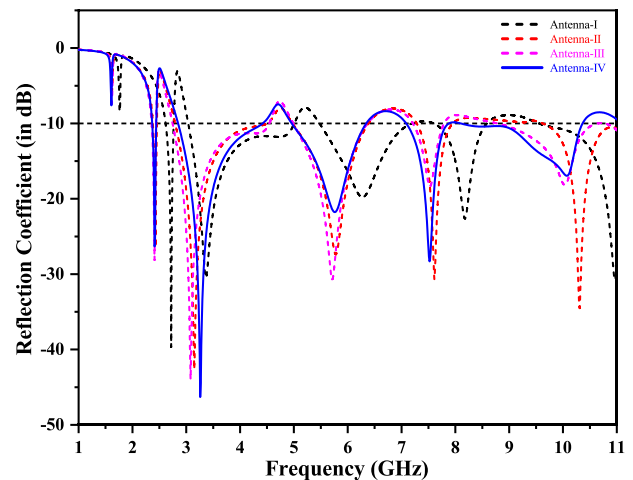


Figure 10. Reflection Coefficient response of different antenna evolution steps.

10 GHz, as shown in Fig. 10. The substrate thickness, size, and other parameters of all four antennas are uniform. The design of

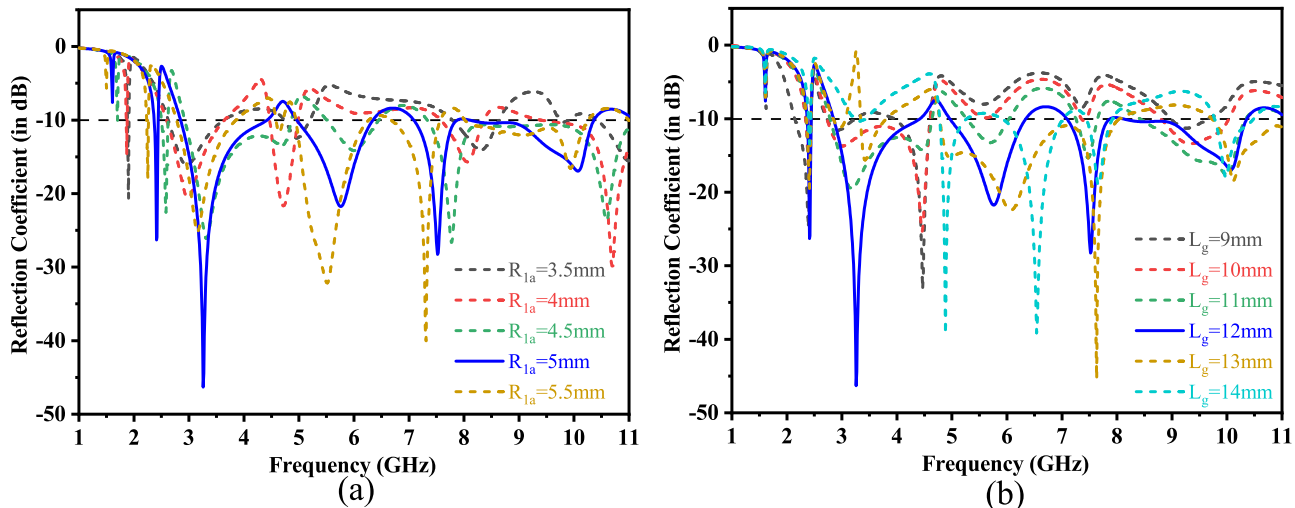


Figure 11. Variation of multiband antenna parameters: (a) Impact of inner heptagon radius (R_{1a}) and (b) Effect of defective ground structure length (L_g).

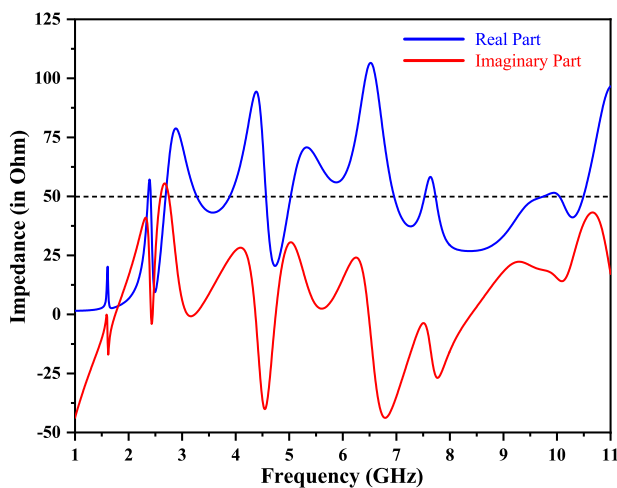


Figure 12. Impedance characteristics of the multiband antenna across multiple frequency bands.

the antenna began with a circular patch antenna for use in wireless frequencies such as the 2.45 GHz ISM band. The first antenna, ANTENNA-I, achieved a multiband response by integrating three circular patches. Subsequently, the circular metallic patches transformed and became nonagon, octagon, and heptagon shapes in successive processes. ANTENNA-II features three polygonal ring-shaped metallic.

The ANTENNA-III takes advantage of the AMC unit cell design by rotating the polygonal metallic patches to broaden the multiband response across all frequencies. The authors did achieve their desired outcome; however, the integration of the AMC surface could have been better. To tackle this issue, ANTENNA-IV presents a novel patch design comprised of seven rectangular patches with dimensions of $L_R \times W_R$. Table 4 compares the performance of each antenna in terms of resonant frequency, impedance bandwidth, and operational frequency band. The results show that these parameters continually improve with each successive step, leading to an impressive -10 dB impedance bandwidth for the proposed antenna.

Investigating the parameters of the multiband antenna

Optimizing the proposed multiband antenna is done by changing specific geometrical parameters to showcase the design's impact on the operating bandwidth. The two crucial parameters are the radius of the inner heptagon (R_{1a}) and the length of the defective ground structure (L_g). Figure 11(a) indicates that the impedance bandwidth decreases as the heptagon radius becomes small. However, a triband response is obtained for radii more significant than 5 mm, causing an increase in impedance bandwidth. Figure 11(b) reveals that altering the L_g value to less than 12 mm significantly changes the impedance bandwidth with either a single-band or dual-band response. For L_g values of 13 and 14 mm, the antenna provides a multiband response with a low impedance bandwidth, which is above the optimal value of L_g . Consequently, after optimization, the optimal $R_{1a} = 5$ mm and $L_g = 12$ mm values result in a broader bandwidth and a more balanced multiband response.

Analysis of the equivalent circuit of the multiband antenna

The proposed antenna was designed using a lumped equivalent circuit consisting of five cascading parallel RLC circuits, each resonating at different frequencies. The appropriate resonances were identified by analyzing the real and imaginary parts of the impedance, with values close to 50 and 0 Ω , respectively, as shown in Fig. 12. The circuit was modeled in ADS software, and its simulation results are shown in Fig. 13. A radio frequency signal was fed to the antenna through a 3.5-mm SMA connector, and a source impedance of 50 Ω was assumed. The lumped component values of the equivalent circuit were determined based on the matching bandwidth premise, using equation (5) and a 50 Ω impedance.

RLC resonant circuit models were used to approximate reflection coefficient drops below -10 dB to create an equivalent circuit model. Real and imaginary impedance values were derived from ANSYS HFSS, based on the condition and displayed in Table 5, along with inductance and capacitance values. The frequency range of 1 to 11 GHz in Fig. 13(b) exhibits five resonant modes. During ADS simulations, the lumped component values were adjusted to achieve the appropriate responses at the corresponding resonant frequencies. However, due to the circuit model being approximately matched to 50 Ω , the component values varied at higher

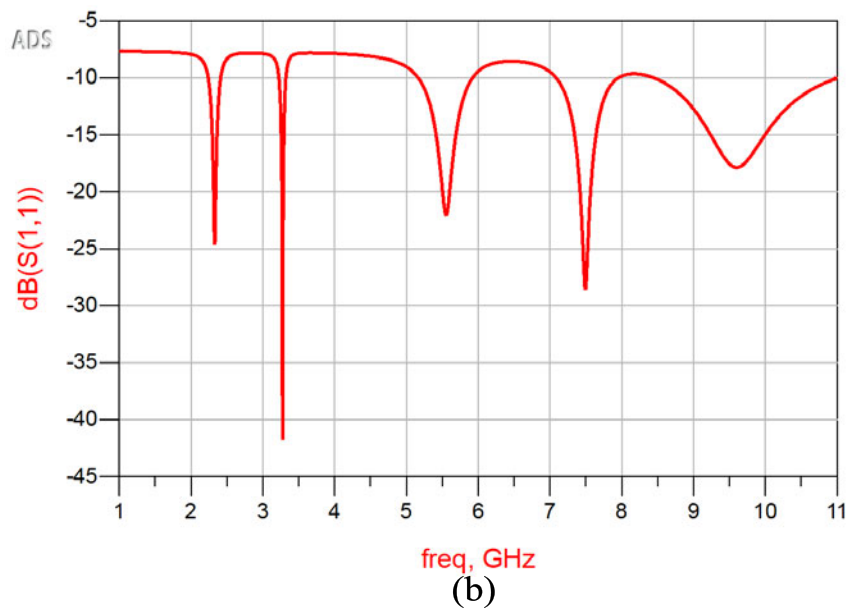
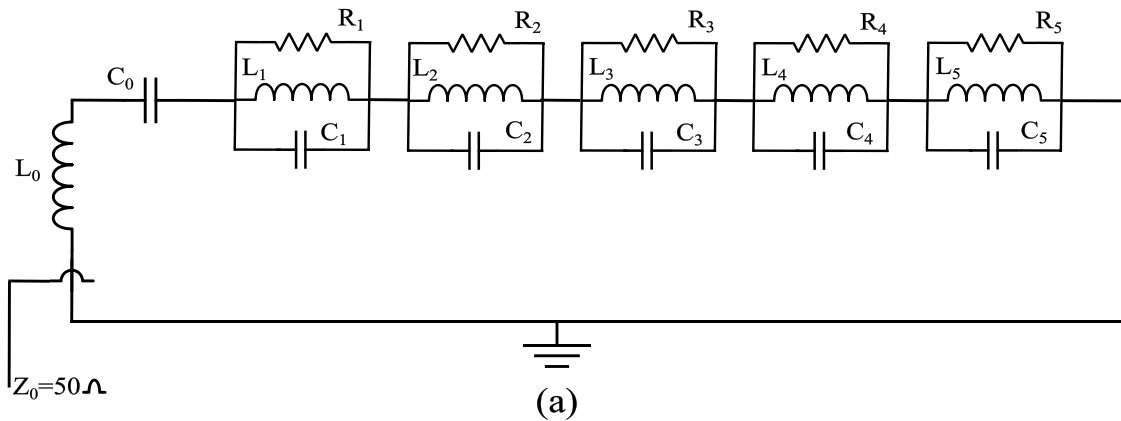


Figure 13. (a) Lumped equivalent circuit model of the multiband antenna, and (b) Reflection coefficient response of the multiband antenna, as simulated in ADS software.

Table 5. Lumped equivalent circuit component values of the multiband antenna

S.No.	Resonant Frequency (GHz)	Impedance (Real Part) (Ω)	Impedance (Imaginary Part) (Ω)	Capacitance (pF)	Inductance (pH)
1	2.4	$R_1 = 50.55$	2.43	$C_1 = 27.190$	$L_1 = 160.56$
2	3.25	$R_2 = 50.15$	0.86	$C_2 = 56.623$	$L_2 = 41.878$
3	5.6	$R_3 = 57.41$	4.52	$C_3 = 6.1268$	$L_3 = 125.17$
4	7.5	$R_4 = 50.51$	4.02	$C_4 = 5.2604$	$L_4 = 85.010$
5	10	$R_5 = 49$	14.15	$C_5 = 1.1175$	$L_5 = 223.75$

frequencies, resulting in a low bandwidth at the second resonant frequency.

Results and discussion of the integrated antenna design

The integrated design of the multiband antenna consists of a 4×4 AMC surface, a foam layer, and the multiband patch antenna itself.

The proposed quad-band 4×4 AMC surface has a central point, with the multiband antenna located $D_{ANT-AMC}$ away from that point. The fabricated antenna and AMC surface are shown in Fig. 14(a) and (b), respectively. The foam layer is a separator between the antenna and the AMC surface, resulting in an overall antenna size of $64 \times 64 \times 16.2 \text{ mm}^3$. The integrated antenna parameters are discussed in this section, including the results obtained in free space and the presence of a human phantom.

Free-space performance of the integrated design

A 4×4 AMC surface was created by repeating the AMC unit cell in two dimensions. The multiband antenna was separated from the AMC surface by a Styrofoam layer in the simulations. At the same time, physical separation was achieved using nonconductive materials such as glue sticks in the prototype. The integrated antenna design was fabricated and shown in Fig. 15 with top and isometric views. The performance of the proposed design was evaluated using a VNA to measure S_{11} and voltage standing wave ratio (VSWR), as shown in Fig. 16(a). Figure 16(b) and (c) displays a screenshot of the S_{11} and VSWR in VNA display. The measured

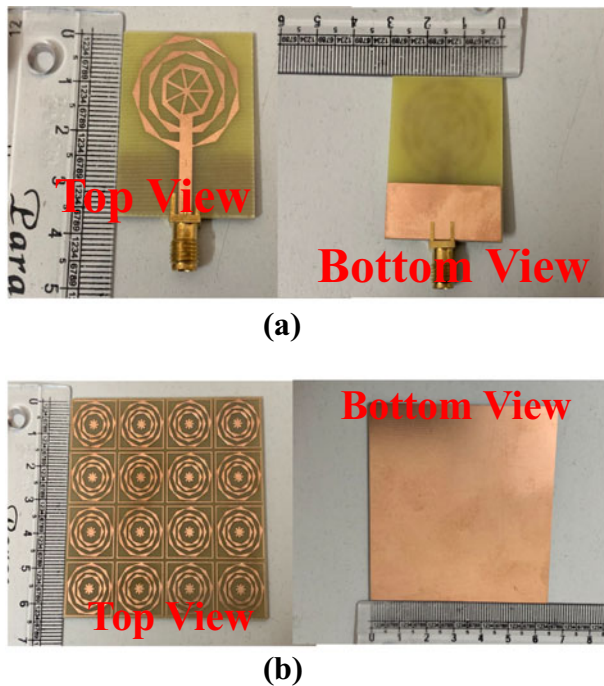


Figure 14. Fabricated prototype: (a) Multiband antenna and (b) 4×4 AMC surface.

S_{11} and VSWR curves after applying the AMC surface are shown in Fig. 17. A comparison between the simulated and measured S_{11} and VSWR of the antenna with and without the AMC surface is presented in Fig. 17(a) and (b), revealing a multiband response. These results show good agreement between the simulation and measurement data. Table 6 compares antenna metrics, including S_{11} , impedance bandwidth, gain, FBR, and back lobe level, with and without the AMC surface.

Figure 18(b) shows the peak gain of the antenna with and without the AMC surface, as determined by simulation and measurement. By incorporating the AMC surface, the antenna's peak gain is enhanced from 5.97 to 8.55 dBi and has consistent gain across the resonant frequency. The maximum gain is achieved at 6.01 GHz. In addition, the AMC surface significantly reduces radiation in the opposite direction. Therefore, the FBR parameter reflects the amount of energy reflected from the antenna. As seen in Fig. 18(a), the AMC plane enhances FBR from 1.5 dB at 4.5 GHz to 31.5 dB. The anechoic chamber depicted in Fig. 19 can determine

the radiation efficiency, gain, pattern, and FBR of an integrated antenna with a 4×4 AMC surface. The antenna's radiation efficiency over its operating band is consistently greater than 88%, as confirmed by both simulation and measurement results. However, slight variations may arise between measured and simulated values due to fabrication, soldering, and the physical separation of the AMC surface and antenna using glue sticks. Nevertheless, the measured and simulated values match nicely within the operating bandwidth.

The anechoic chamber measurements of the integrated antenna design's normalized radiation patterns are depicted in Fig. 19. To further analyze the radiation properties of the design, Fig. 20 compares the simulated and measured radiation patterns in the XZ and YZ planes at frequencies of 2.4, 3.2, 5.5, 7.5, and 10 GHz. The integrated design displays a unidirectional radiation pattern with suppressed rear lobe magnitude and enhanced main lobe gain in both planes. While the radiation pattern at the five resonant frequencies without AMC appears almost omnidirectional, the integrated design achieves rear lobe alleviation, decreasing the magnitude of the rear lobe from -0.0053 to -6.3889 dBi at 2.4 GHz. Table 6 summarizes the gains achieved by the integrated design at the resonant frequencies. Compared to the antenna without AMC, the gains at 2.4, 3.2, 5.5, 7.5, and 10 GHz improve by 3.99, 5.13, 2.66, 1.09, and 1.52 dB.

Figure 21 illustrates the surface current distributions of the integrated antenna at different resonant frequencies, providing valuable insights into the antenna's design behavior and the determinants of its resonant frequency. At the lower resonance frequency of 2.4 GHz for the suggested design, Fig. 21(a) reveals a major current distribution along both the feed line and the octagonal ring. Figure 21(b) showcases the surface current distributions at 3.2 GHz, vividly demonstrating the significant current concentration along the feedline and the outer nonagon and octagon rings. At the resonant frequency of 5.5 GHz, a pronounced surface current concentration is observed exclusively at the center of the radiating patch. Figure 21(d) depicts the surface current distribution at 7.5 GHz, revealing that a significant portion of the current flows through the outer polygonal ring, converging at the center point of the radiating patch. The surface current is uniformly distributed across the radiating patch at the higher resonance frequency.

Analysis of the integrated design performance with varying AMC surface configurations

The integrated design's impedance bandwidth is closely linked to the array size of the AMC surface, the distance between the antenna

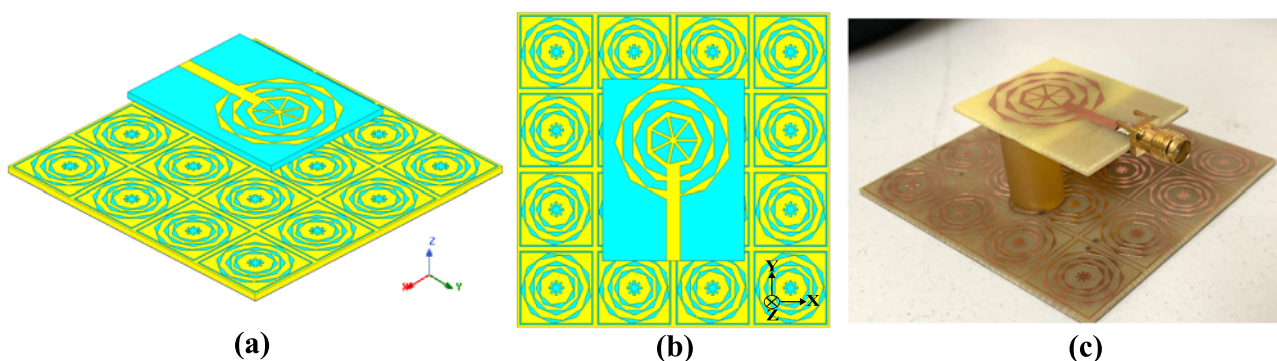


Figure 15. Perspectives of integrated design: (a) Isometric view, (b) top view, and (c) isometric view of the prototype.

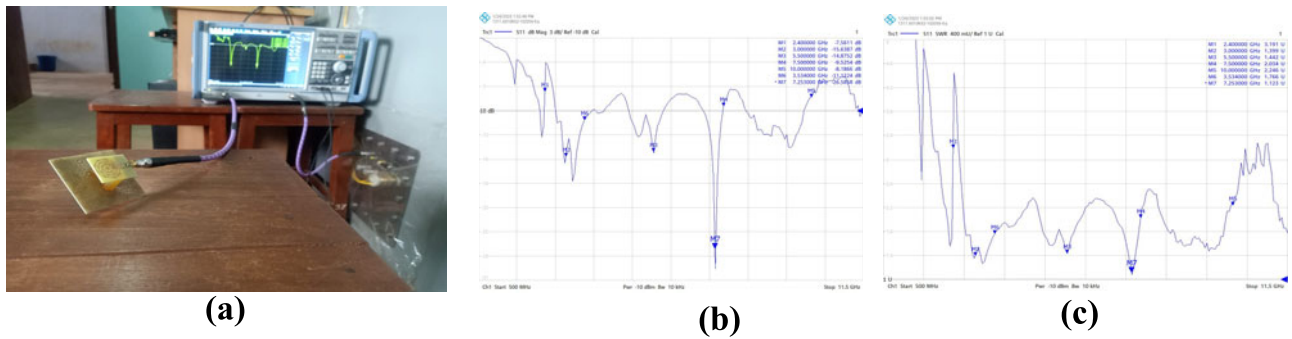


Figure 16. VNA measurement configuration and results for the integrated design: (a) VNA setup with integrated design; screenshot of VNA display (b) S_{11} and (c) VSWR curves.

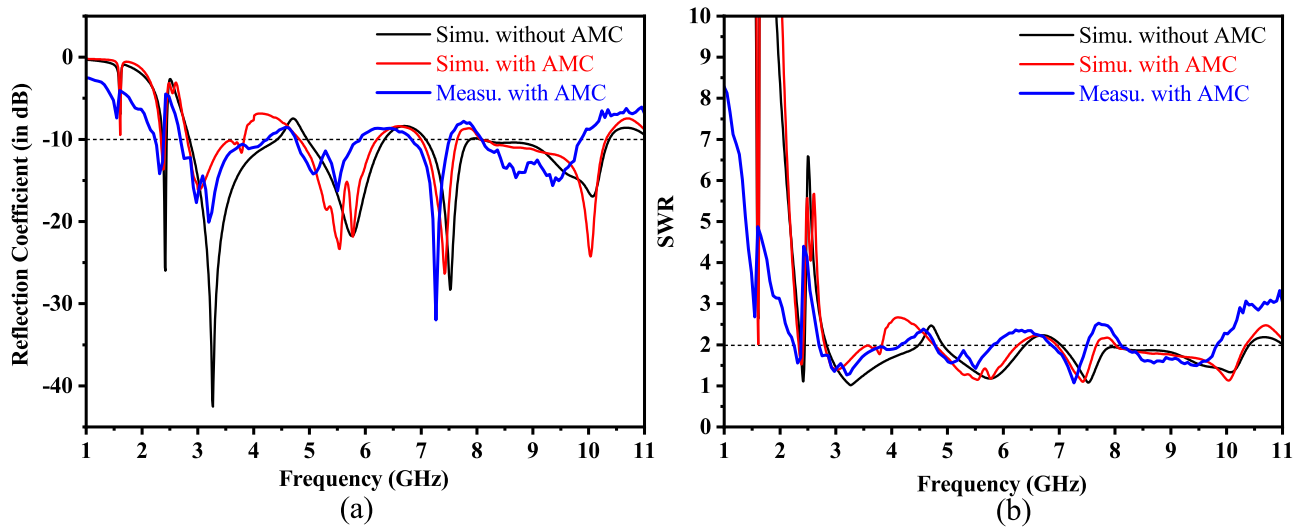


Figure 17. Simulated and measured results of the antenna with and without the AMC surface: (a) S_{11} and (b) VSWR.

Table 6. The impact of AMC surface introduction on antenna performance

Resonant Frequency (Band)	Operating Frequency (GHz)	S_{11} (dB)	-10 dB Impedance Bandwidth (%)	Gain(dB)	FBR(dB)	Back Lobe Level (dBi)
1	Without AMC	2.37–2.44	-26.4	2.91	1.61	0.46
	Simulated with AMC	2.34–2.43	-13.69	3.77	6	13.05
	Measured with AMC	2.26–2.4	-13.2	6.09	4.61	12.02
2	Without AMC	2.85–4.42	-46.30	43.19	2.58	0.78
	Simulated with AMC	2.81–3.83	-15.65	30.72	7.6	14.35
	Measured with AMC	2.71–3.8	-18.8	33.49	7.11	10.05
3	Without AMC	4.96–6.35	-21.75	24.58	4.88	0.39
	Simulated with AMC	4.82–6.21	-24.1	25.20	7.5	15.03
	Measured with AMC	4.8–5.77	-15.2	18.35	7.12	16.82
4	Without AMC	7.08–7.88	-28.28	10.69	0.81	4.21
	Simulated with AMC	7–7.65	-26.35	8.87	6.17	7.60
	Measured with AMC	6.94–7.58	-30.1	8.82	1.81	6.41
5	Without AMC	8.07–10.37	-16.94	24.95	4.47	0.62
	Simulated with AMC	8.06–10.31	-24.25	24.5	6.4	10.03
	Measured with AMC	8.15–10.1	-14.6	21.37	5.71	12.95

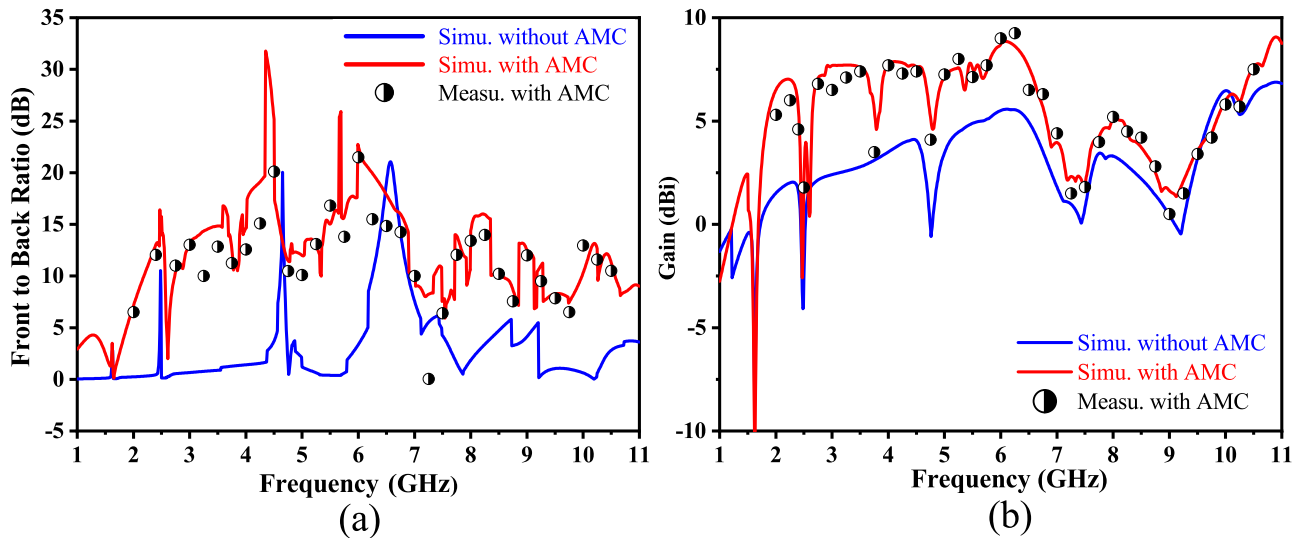


Figure 18. Simulated and Measured results with and without AMC surface: (a) Front-to-back ratio and (b) gain.

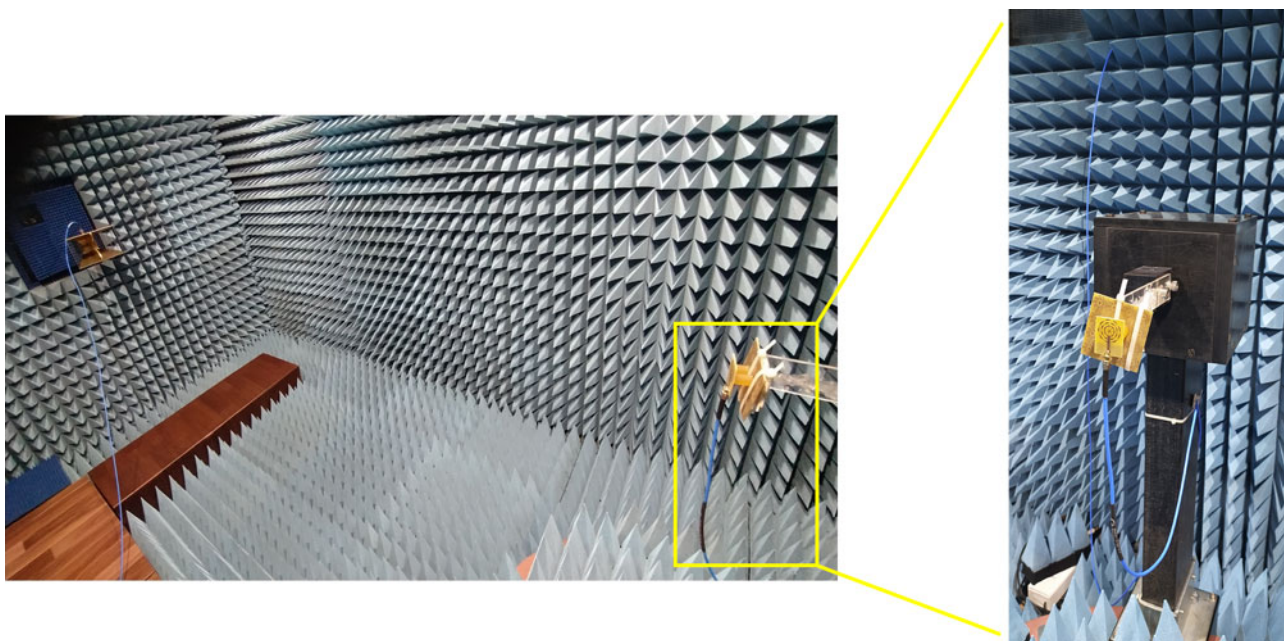


Figure 19. The integrated antenna design setup in an anechoic chamber.

and the surface, and the antenna's orientation concerning the AMC surface axis. As a result, it is essential to consider these factors when mounting antennas on AMC.

Depending on the antenna dimensions, the AMC array can range from 3×3 to 5×5 . Irrespective of the array shape, the antenna is situated above the $D_{\text{ANT-AMC}}$ distance and is centered relative to the AMC surface. All possible array sizes are depicted in Fig. 22, and Table 7 compares their gain and bandwidth at five different resonance frequencies. Even though the antenna's reflection coefficients remain stable across a range of AMC array sizes, its performance improves significantly with increasing array size. At the first and last resonance frequencies, there is a minor gain reduction in a 5×5 array. To achieve a balance between reflection coefficients, integrated design size, gain, and production cost, the recommended AMC plane design employs a 4×4 unit cell,

as shown in Fig. 23(b), which exhibits the reflection coefficient response for all AMC array size variations.

The multiband antenna, situated at the height of $D_{\text{ANT-AMC}}$ above the center of the AMC surface, is designed to provide coverage across a wide range of frequencies. Figure 23(a) illustrates the effects of varying the $D_{\text{ANT-AMC}}$ parameter on the antenna's performance. There is no denying that $D_{\text{ANT-AMC}}$ has a significant impact on the impedance bandwidth of the AMC-backed antenna. The optimal distance is determined by varying the $D_{\text{ANT-AMC}}$ parameter between 9 and 17 mm. A $D_{\text{ANT-AMC}}$ of 13 or 15 mm enables the system to take advantage of the antenna's multiband capabilities, with smaller values unable to cover the multiband response. By balancing radiation performance and profile requirements, a fair $D_{\text{ANT-AMC}}$ value of 13 mm is determined to effectively cover most wireless frequency bands using the AMC-backed antenna.

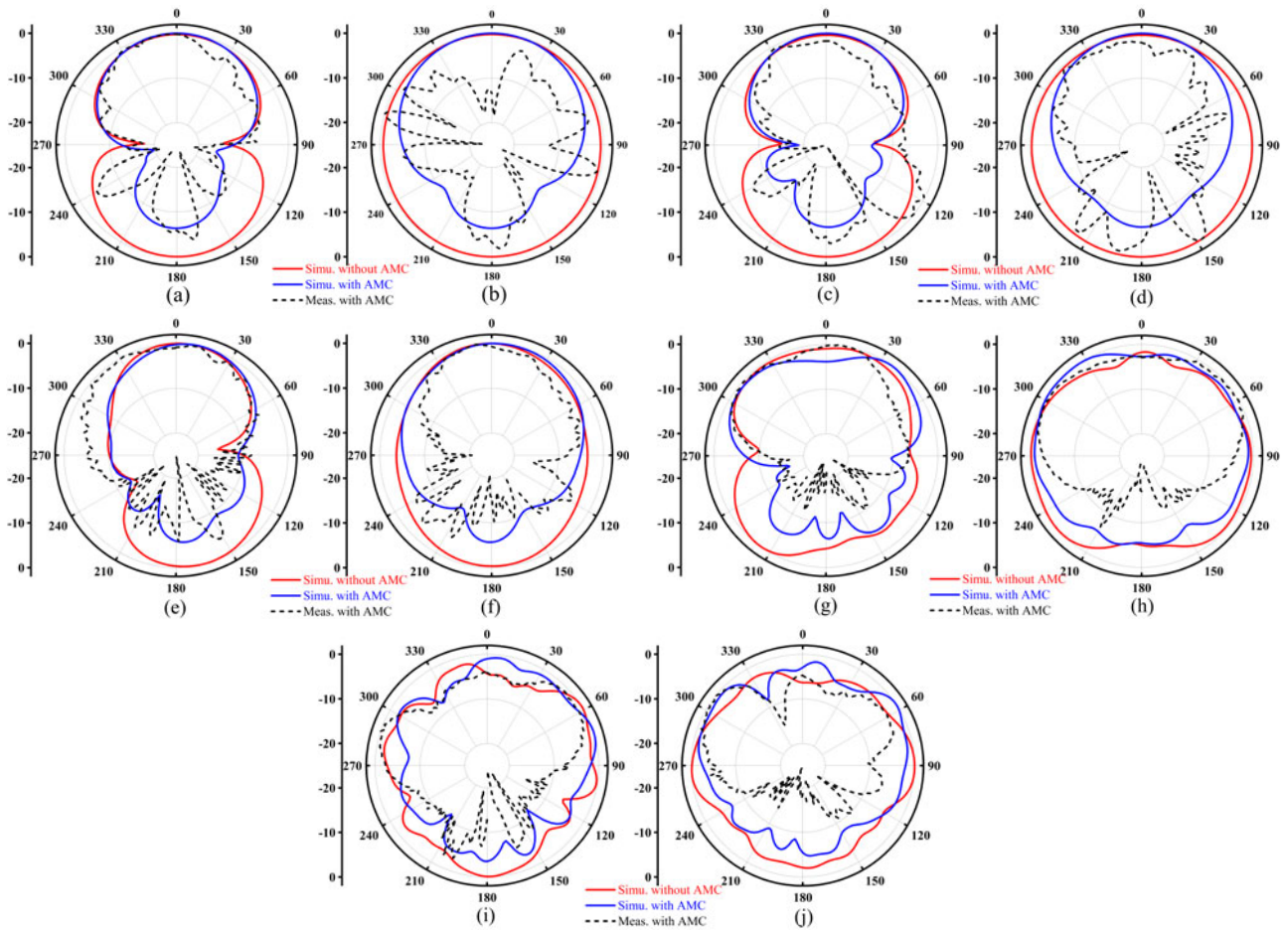


Figure 20. Comparison of measured and simulated radiation patterns in XZ plane at (a) 2.4 GHz, (c) 3.2 GHz, (e) 5.5 GHz, (g) 7.5 GHz, and (i) 10 GHz and YZ plane at (b) 2.4 GHz, (d) 3.2 GHz, (f) 5.5 GHz, (h) 7.5 GHz, and (j) 10 GHz.

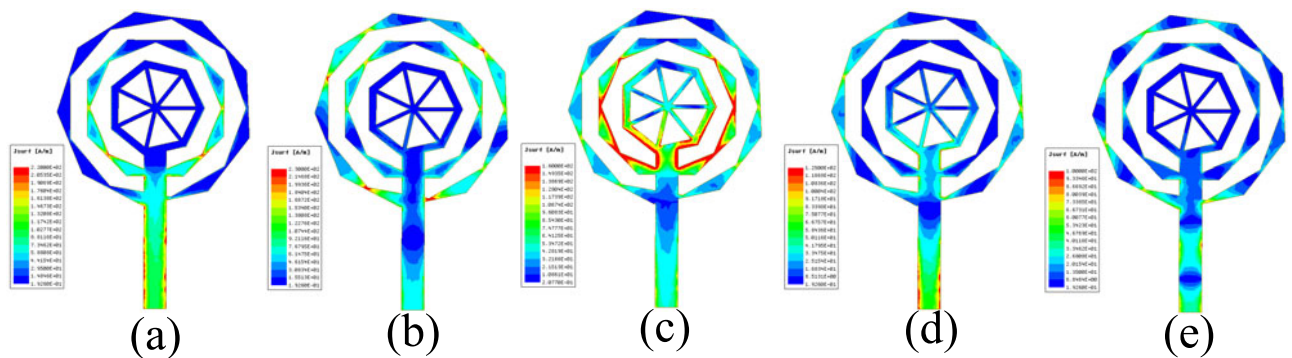


Figure 21. Surface current distribution of the integrated antenna at (a) 2.4 GHz, (b) 3.2 GHz, (c) 5.5 GHz, (d) 7.5 GHz, and (e) 10 GHz.

Figure 24(a) shows the orientation angle of the antenna relative to the AMC plane. At the same time, Fig. 24(b) presents the reflection coefficients of the integrated design at various orientation angles denoted by the symbol “ θ .” The orientation angle ranges from 0° to 90° in 15-degree increments. As a result, the integrated design generates a multiband response at frequencies of 2.5, 3.2, 5.5, 7.5, and 10 GHz, providing acceptable variation coverage. The antenna response at 0- and 90-degree orientation angles is identical due to the symmetrical AMC surfaces. Consequently, all

orientations provide the same impedance bandwidth inside each band.

Analysis of integrated design performance in the presence of a human phantom

The distance between the antenna and a human phantom is a critical parameter to consider when designing WBAN antennas. In paper [8], the impact of this distance on antenna performance

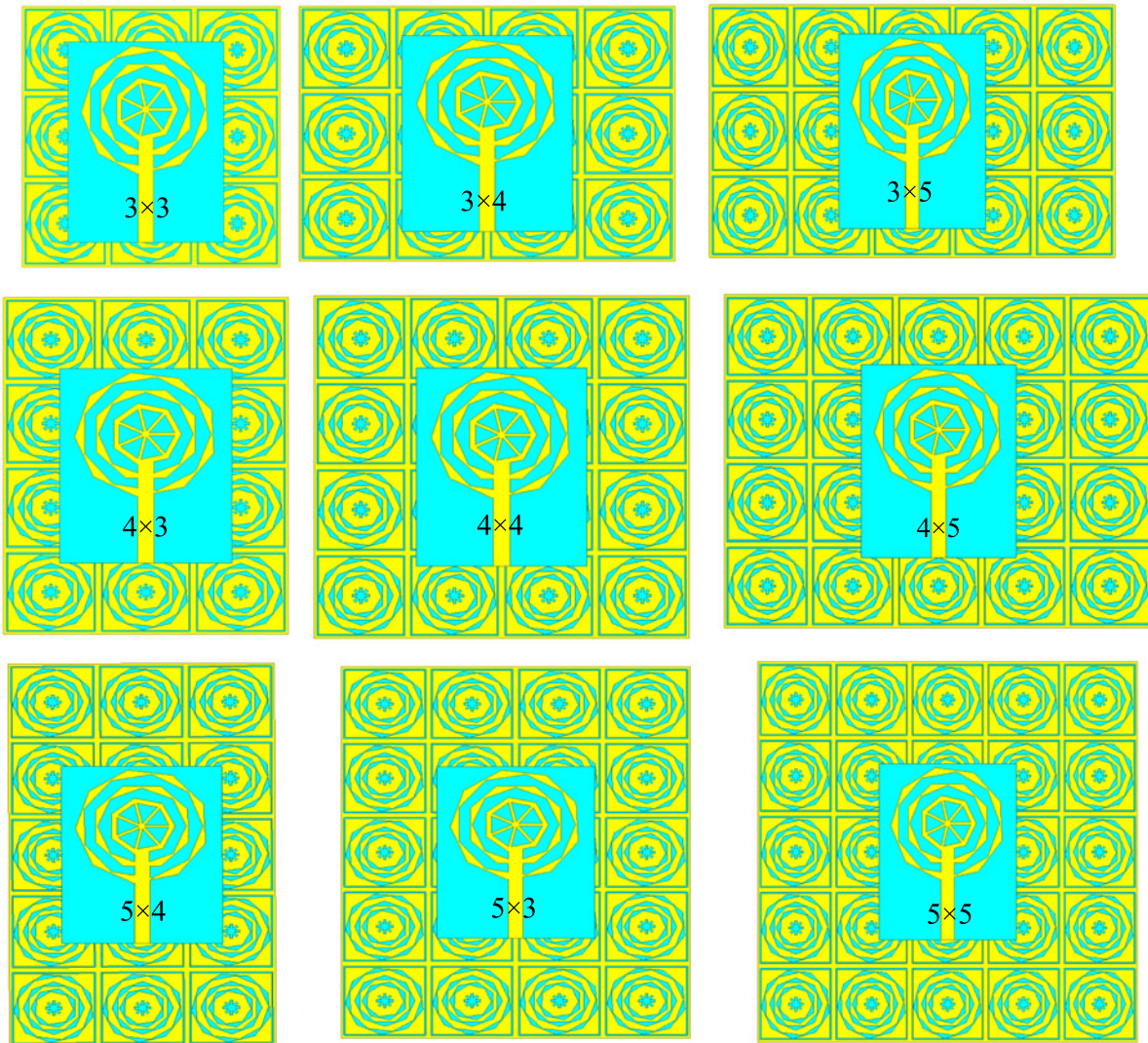


Figure 22. Antenna with different array size.

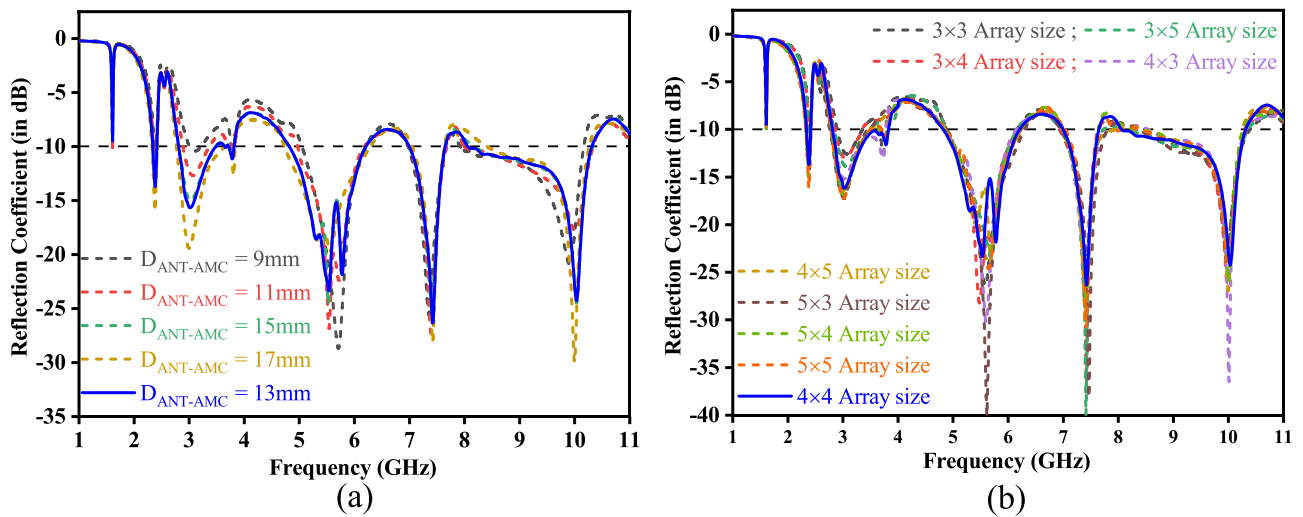


Figure 23. Reflection coefficient response (a) for different $D_{ANT-AMC}$ and (b) for different array variation.

Table 7. Effects of different AMC array sizes on antenna gain and bandwidth (BW) at five resonance frequencies

AMC Array Size	First Resonance		Second Resonance		Third Resonance		Fourth Resonance		Fifth Resonance	
	Freq. Band (GHz) (BW %)	Gain	Freq. Band (GHz) (BW %)	Gain	Freq. Band (GHz) (BW %)	Gain	Freq. Band (GHz) (BW %)	Gain	Freq. Band (GHz) (BW %)	Gain
3 × 3	2.39–2.41 (0.83)	6.2	2.89–3.36 (15.04)	5.1	4.88–6.17 (23.35)	6.8	7–7.65 (8.88)	5.9	8.31–10.39 (22.25)	5.8
3 × 4	2.39–2.41 (0.83)	8.2	2.86–3.35 (15.78)	8.3	4.9–6.23 (23.90)	7.4	6.93–7.04 (9.75)	5.6	8.44–10.34 (20.23)	4.2
3 × 5	2.38–2.41 (1.25)	2	2.84–3.48 (20.25)	5	4.88–6.17 (23.35)	6.6	6.96–7.73 (10.48)	8.2	8.03–10.35 (25.25)	1.16
4 × 3	2.34–2.42 (3.36)	6.3	2.81–3.78 (29.44)	5.7	4.85–6.15 (23.63)	7	6.99–7.95 (12.85)	5.2	8.54–10.32 (18.87)	5
4 × 4	2.34–2.43 (3.77)	6	2.81–3.83 (30.72)	7.6	4.82–6.21 (25.20)	7.5	7–7.65 (8.87)	6.17	8.06–10.31 (24.5)	6.4
4 × 5	2.34–2.41 (2.95)	7.4	2.78–3.5 (22.93)	7.7	4.85–6.27 (25.54)	6.3	7–7.94 (12.58)	5.3	8.44–10.25 (19.37)	5.7
5 × 3	2.33–2.42 (3.78)	9.2	2.76–3.46 (22.50)	11	4.84–6.3 (26.21)	7.4	6.95–7.81 (11.65)	7.2	8.36–10.31 (20.89)	4.3
5 × 4	2.33–2.42 (3.78)	3	2.79–3.49 (22.29)	5.9	4.84–6.22 (24.95)	7.6	6.99–7.64 (8.88)	7	8.24–10.27 (21.93)	2
5 × 5	2.32–2.42 (4.22)	3.24	2.78–3.51 (23.21)	6.09	4.85–6.22 (24.75)	6.68	7.03–7.66 (8.57)	7.6	8.41–10.03 (17.57)	2.4

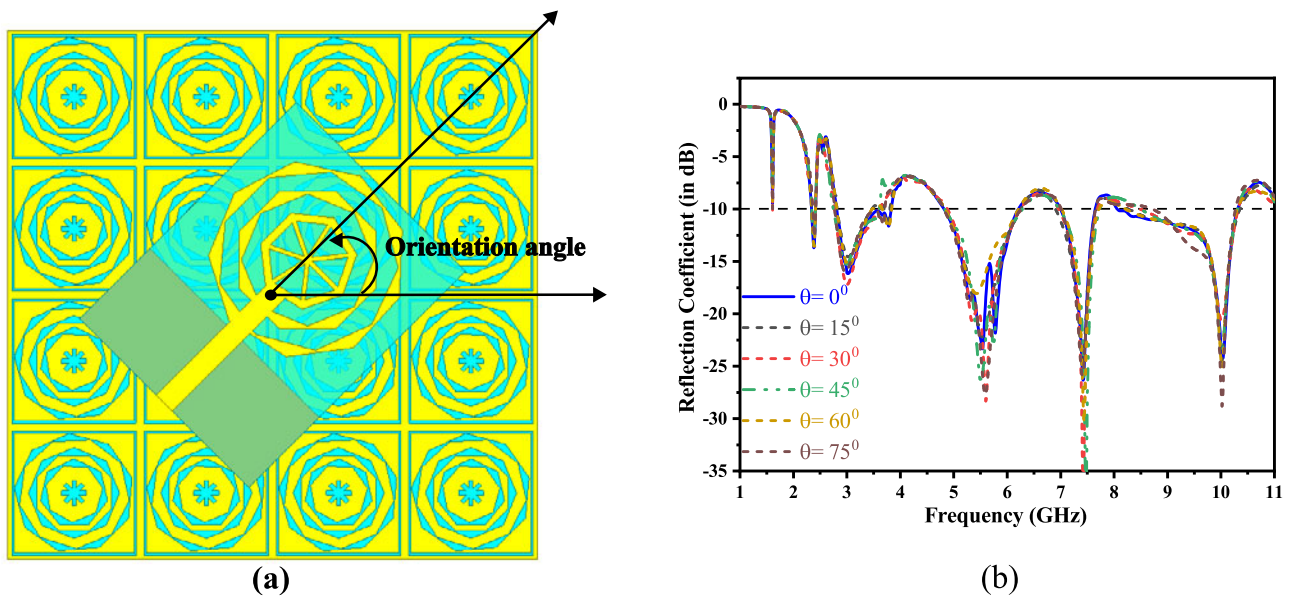


Figure 24. (a) The arrangement of orientation angles and (b) The reflection coefficient response for various orientation angles.

is studied, and it is recommended to maintain a gap of 3 mm between the antenna and the phantom to ensure optimal performance. Additionally, when designing antennas for use in WBANs, it is essential to evaluate their SAR to ensure they are safe for human use. The SAR quantifies the amount of electromagnetic power that the human body absorbs and can be used to determine whether a given antenna design poses any risk to human health. The SAR level is calculated using equation (8), where σ , ρ , and \vec{E} are tissue conductivity, mass density, and electric field, respectively.

$$SAR = \frac{\sigma |\vec{E}|^2}{\rho} \tag{8}$$

Figures 25 and 26 present the simulated and measured reflection coefficient responses of the proposed antenna in the presence of a human phantom, comparing the cases with and without an AMC surface, respectively. The proposed antenna is suitable for off-body communication in WBAN applications. It can be used on

purses and textile pockets as it is unaffected by human loading, thus ensuring the impedance bandwidth and gain remain stable. The SAR of the antenna is a critical factor to consider when designing wearable technology, and it is assessed using an HFSS simulation with a human phantom that includes a hand, arm, and leg with an input power of 100 mW. Figure 27 demonstrates the positioning of the antenna and AMC surface, placed within 3 mm of the phantom, as depicted in both the simulation and measurement setups. Figure 28 depicts the maximum and minimum SAR values at different resonant frequencies for various human phantom configurations. The average SAR values of the antenna without an AMC surface are illustrated in Fig. 28(a). Wearable technology must have SAR values of less than 1.6 W/kg. Figure 28(b) shows the cumulative SAR values with the presence of the AMC surface, which leads to a significant decrease in SAR. Table 8 reveals that the maximum SAR value drops from 18.7261 to 0.0627 W/kg when the AMC surface is included.

Table 9 presents a performance comparison between the proposed antenna and several existing antennas for off-body

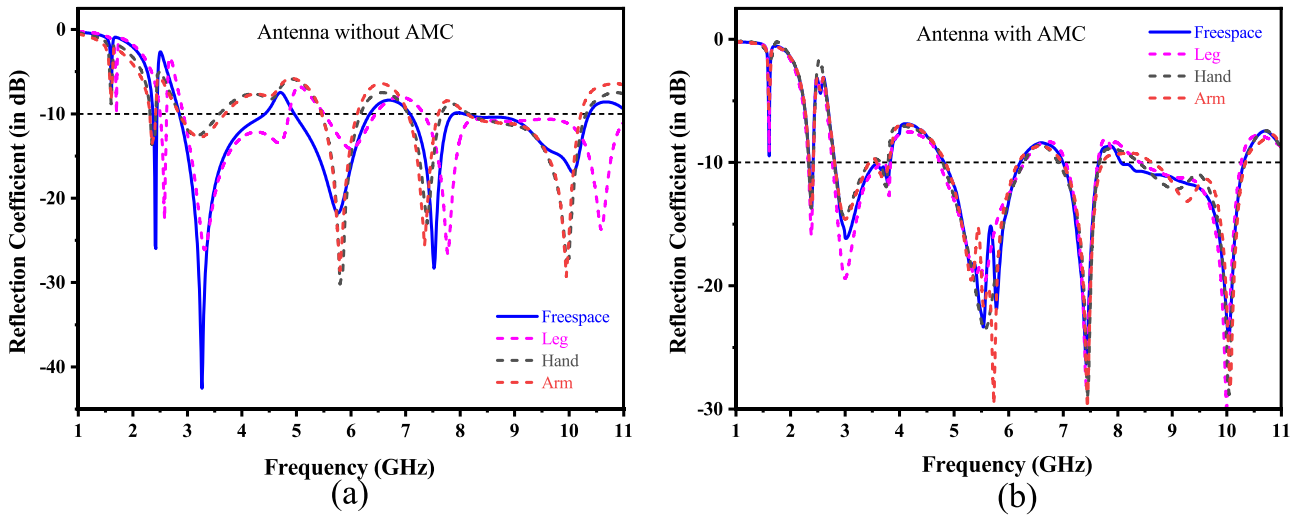


Figure 25. Simulated reflection coefficient response with human phantom: (a) Antenna without AMC and (b) antenna with AMC.

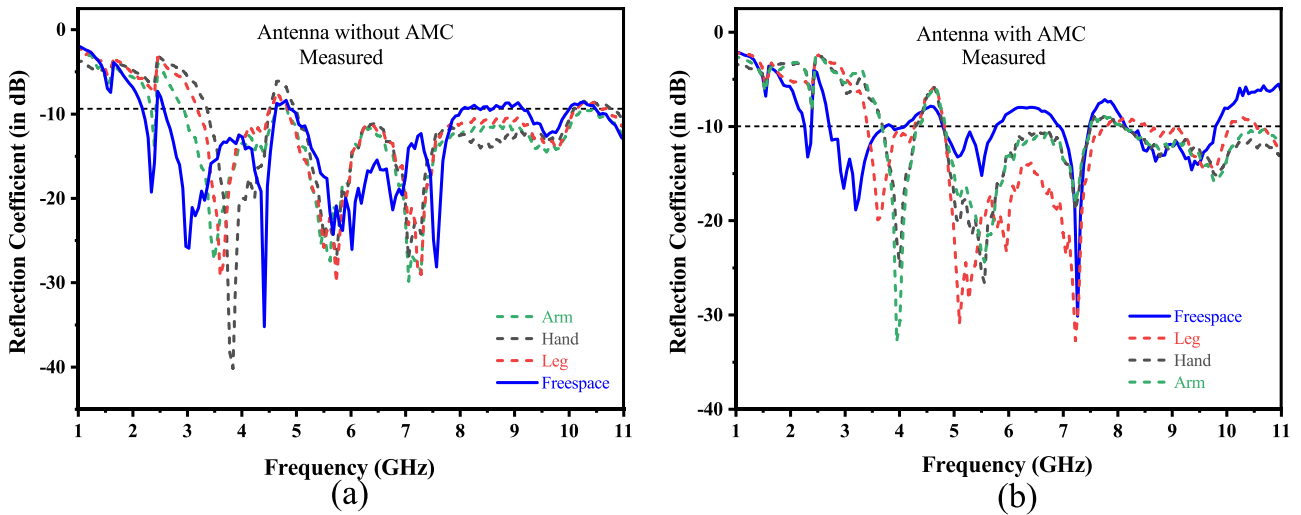


Figure 26. Measured Reflection coefficient response with human phantom: (a) Antenna without AMC and (b) antenna with AMC.

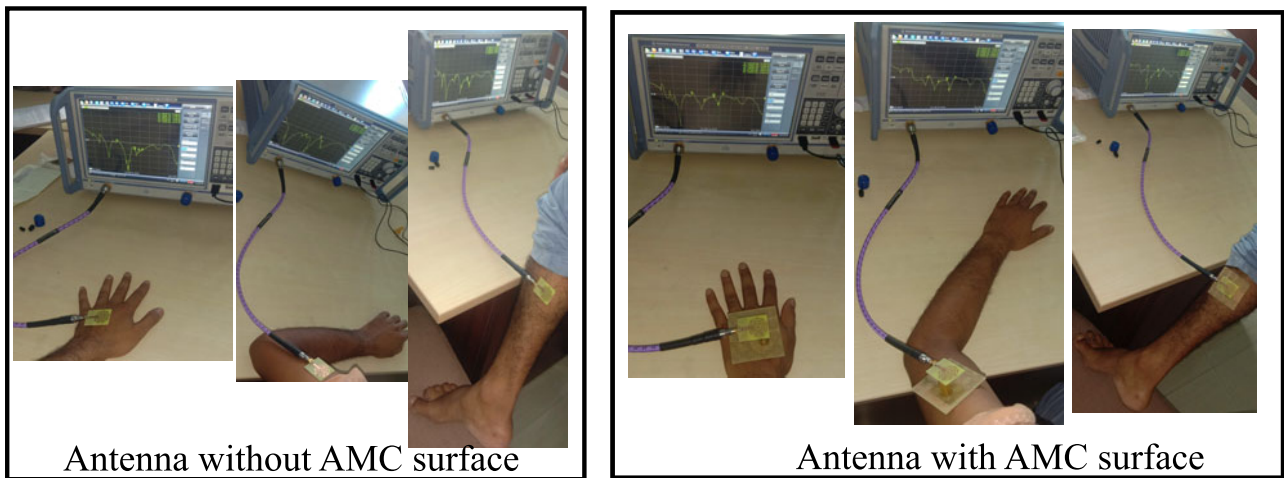


Figure 27. Measurement of antenna parameters with human phantom.

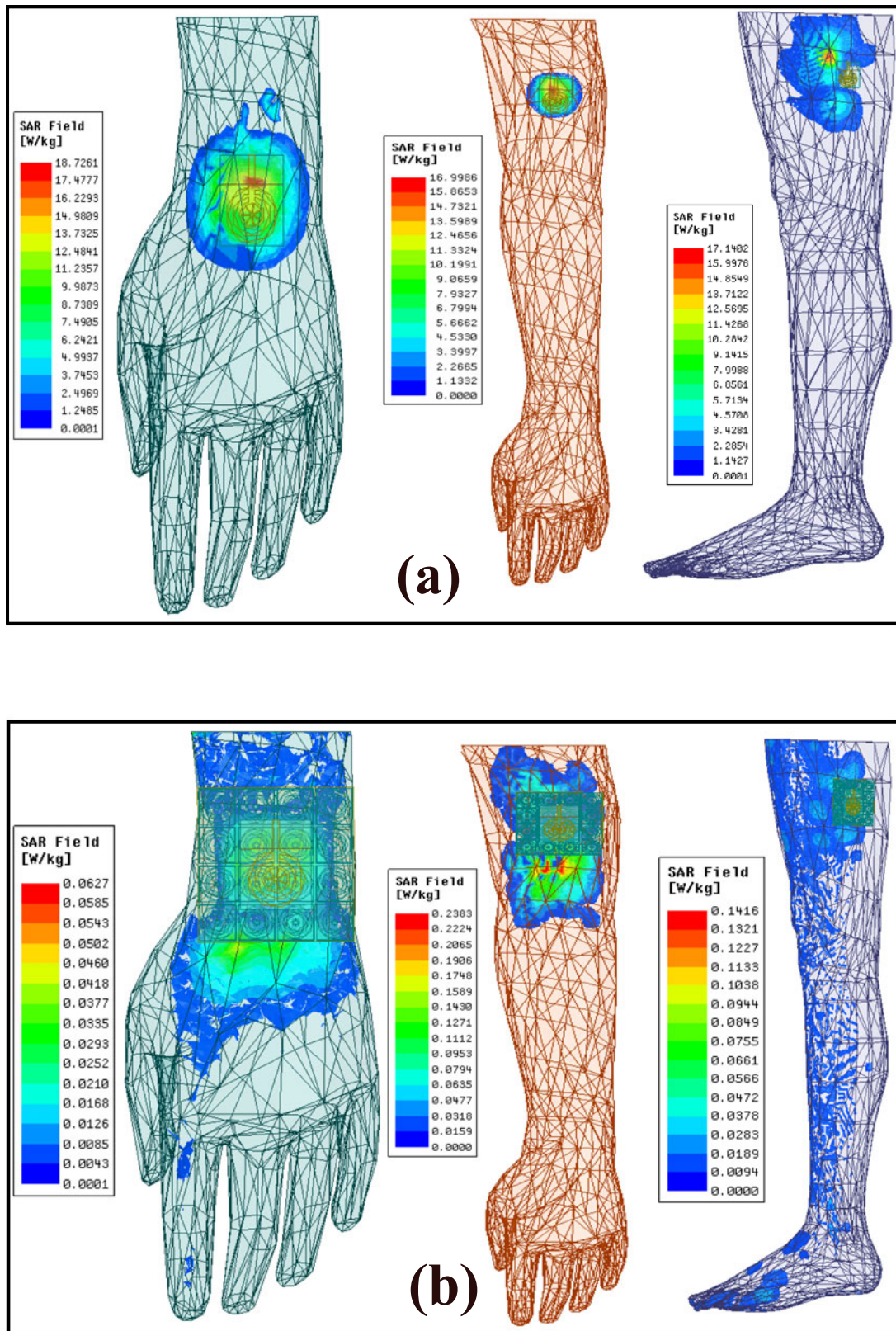


Figure 28. (a) Maximum SAR values without AMC and (b) Minimum SAR values with AMC.

communication. Although most of the reviewed literature uses FR4 substrate materials, other materials are also discussed. The proposed antenna outperforms other antenna designs in the literature

due to its multiband response and five different resonance frequencies. Although the first resonance has less impedance bandwidth, the proposed antenna is smaller than that in papers [5, 28, 29] and

Table 8. SAR values comparison of the proposed design

Human Phantom Model		First Resonance		Second Resonance		Third Resonance		Fourth Resonance		Fifth Resonance	
		Value	Reduction (%)	Value	Reduction (%)	Value	Reduction (%)	Value	Reduction (%)	Value	Reduction (%)
Hand	Without AMC	13.6468	99.53	15.5124	94.57	5.4690	93.37	18.7261	94.53	4.8059	84.70
	With AMC	0.0627		0.8432		0.3628		1.0237		0.7352	
Arm	Without AMC	12.6229	95.72	16.9986	98.53	15.2215	96	9.9507	96.48	14.6877	98.38
	With AMC	0.5400		0.2504		0.6088		0.3506		0.2383	
Leg	Without AMC	17.1402	99.16	11.4522	98.56	16.3332	97.12	13.8914	96.29	10.9998	98.71
	With AMC	0.1439		0.1646		0.4709		0.5147		0.1416	

Table 9. Comparison with previous works

References	Size of the Antenna (mm ³)	No. of Bands	Operating Frequency/Band (GHz)	Gain (dBi)	FBR (dB)	SAR (W/Kg)	Substrate Material	AMC Array Size	Efficiency (%)
[4]	61.5 × 61.5 × 12.2	2	2.45 5.80	5.676.59	–	0.35 0.39	Polyimide substance	3 × 3	90
[5]	23 × 74 × 6	1	2.4	4.5	14	0.02	denim	2 × 4	85.6
[6]	34.4 × 34.4 × 4.016	1	5.8	7.6	35.2	0.0264	Rogers RT Duroid 5880	2 × 2	94.69
[13]	32.8 × 32.8 × 6.8	1	5.5–6.96	8.2	–	–	Taconic TLT & FR4	4 × 8	93
[18]	62 × 62 × 7	2	3.5 5.8	6.65.9	18.7 21.3	0.128 0.043	Textile	3 × 3	60.2 50
[21]	60 × 60 × 33.7	3	2.22–2.49 2.94–4.96 5.41–6.62	4.224.426.44	–	–	FR4	4 × 3	–
[23]	59.88 × 59.88 × 7.524	1	5.5	9.9	25	–	FR4	6 × 6	>70
[27]	57.5 × 57.5 × 5.7	1	2.45	7.63	11.4	0.07	Rogers 3850	2 × 2	96.4
[28]	89 × 83 × 7	1	2.4	6.4	–	0.29	Rogers RO 3003	3 × 3	–
[29]	90 × 90 × 26.2	4	2.45 3.5 4.6 5.8	5.2976.46.7	–	–	FR4	5 × 5	–
Proposed work	64 × 64 × 16.2	5	2.4 3.2 5.5 7.5 10	67.67.56.176.4	13.05 14.35 15.03 7.60 10.03	0.0627 0.1646 0.3628 0.3506 0.1416	FR4	4 × 4	>88

comparable in size to papers [4, 18, 21, 23], with even less thickness than in papers [21, 29]. The proposed antenna also achieves a higher gain than all other antennas except papers [13, 23], and has a maximum FBR of 31.5 dB at 6.01 GHz, exceeding all other papers except paper [6]. Furthermore, the proposed antenna has a lower maximum SAR than all other antennas, except paper [6]. The research paper demonstrates the use of metallic hexagonal patches for achieving multiband resonance on a single-layer patch, resulting in a simple and effective antenna design approach that achieves high gain, low SAR, high FBR, and increased bandwidth using a 4 × 4 AMC surface for off-body communication applications.

Conclusion

This study presents a novel multiband antenna design that utilizes a 4 × 4 AMC surface to achieve high gain and low SAR.

The integrated antenna design covers a broad frequency range from 2 to 10 GHz and provides five resonant frequencies at 2.4, 3.2, 5.5, 7.5, and 10 GHz, and the AMC surface generates four zero-degree reflection phases. The design was simulated using ANSYS HFSS and validated using ADS software, and its performance results are confirmed through experimental verification by using a VNA and an anechoic chamber. The results show excellent performance, with a peak gain of 8.55 dBi and a high FBR of 31.5 dB. SAR simulations are performed using hand, arm, and leg phantoms, and the results indicate that the AMC surface effectively reduces SAR by 96.11%. AMC technology significantly reduces SAR levels and improves overall radiation efficiency by nearly 88%. The integrated design is ideal for off-body communication applications and potentially impacts the future of the wearable communication devices.

Acknowledgements. The authors would like to thank Mr. Susovan Ghosh, technical assistant of the National Institute of Technology Agartala, for his assistance in affixing the antenna to the AMC surface and SMA connector.

Author contributions. The research methodology, implementation, simulation, and manuscript preparation were spearheaded by R.V. D.G contributed significantly by providing conceptualization and offering supervision. The manuscript underwent collective review and writing efforts, with all authors making equal contributions to its refinement.

Funding statement. This research received no specific grant from any funding agency, commercial or not-for-profit sectors.

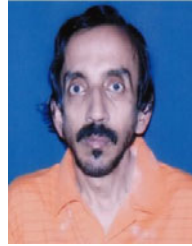
Competing interests. The authors report no conflict of interest.

References

- Bhattacharjee S, Maity S, Chaudhuri SRB and Mitra M (2019) A compact dual-band dual-polarized omnidirectional antenna for on-body applications. *IEEE Transactions on Antennas and Propagation* **67**, 5044–5053.
- Wei K, Li JY, Wang L, Xu R and Xing ZJ (2017) A new technique to design circularly polarized microstrip antenna by fractal defected ground structure. *IEEE Transactions on Antennas and Propagation* **65**, 3721–3725.
- Contopanagos HF (2020) A broadband polarized artificial magnetic conductor metasurface. *Journal of Electromagnetic Waves and Applications* **34**, 1823–1841.
- Wang S and Gao H (2022) A dual-band wearable conformal antenna based on artificial magnetic conductor. *International Journal of Antennas and Propagation* **2022**, 1–8.
- Pathan TU and Kakde B (2022) A compact circular polarized MIMO fabric antenna with AMC backing for WBAN applications. *Advanced Electromagnetics* **11**, 26–33.
- Chaouche YB, Nedil M, Mabrouk IB and Ramahi OM (2022) A wearable circularly polarized antenna backed by AMC reflector for WBAN communications. *IEEE Access* **10**, 12838–12852.
- Abbas MH, Singh S, Sharma A and Gangwar D (2023) Low-profile high gain circularly polarized CRLH transmission line inspired antenna with artificial magnetic conductor for wearable applications. *International Journal of Microwave and Wireless Technologies* **15**(7), 1223–1232.
- Chen Y, Liu X, Fan Y and Yang H (2022) Wearable wideband circularly polarized array antenna for off-body applications. *IEEE Antennas and Wireless Propagation Letters* **21**, 1051–1055.
- Lin C-H, Saito K, Takahashi M and Ito K (2012) A compact planar inverted-F antenna for 2.45 GHz on-body communications. *IEEE Transactions on Antennas and Propagation* **60**, 4422–4426.
- Del-Rio-Ruiz R, Lopez-Garde J-M, Legarda J, Caytan O and Rogier H (2021) A combination of transmission line models as design instruments for electromagnetically coupled microstrip patch antennas in the 2.45 GHz ISM band. *IEEE Transactions on Antennas and Propagation* **69**, 550–555.
- Benkhadda O, Saih M, Chaji K, Ahmad S and Reha A (2022) A compact dual-band CPW-fed slot monopole antenna for WiFi, WLAN and WiMAX applications. *Arabian Journal for Science and Engineering*, 48.
- Verma A, Arya RK and Raghava SN (2023) Metasurface superstrate beam steering antenna with AMC for 5G/WiMAX/WLAN applications. *Wireless Personal Communications* **128**, 1153–1170.
- Malekpoor H, Abolmasoumi A and Hamidkhani M (2022) High gain, high isolation, and low-profile two-element MIMO array loaded by the Giuseppe Peano AMC reflector for wireless communication systems. *IET Microwaves, Antennas & Propagation* **16**, 46–61.
- Paracha KN, Rahim SKA, Soh PJ, Kamarudin MR, Tan K-G, Lo YC and Islam MT (2019) A low profile, dual-band, dual polarized antenna for indoor/outdoor wearable application. *IEEE Access* **7**, 33277–33288.
- Yang X, Ji Y, Ge L, Zeng X, Wu Y and Liu Y (2020) A dual-band radiation-differentiated patch antenna for future wireless scenes. *IEEE Antennas and Wireless Propagation Letters* **19**, 1007–1011.
- Jagtap S, Chaudhari A, Chaskar N, Kharche S and Gupta RK (2018) A wideband microstrip array design using RIS and PRS layers. *IEEE Antennas and Wireless Propagation Letters* **17**, 509–512.
- Gao G-P, Yang C, Hu B, Zhang R-F and Wang S-F (2019) A wearable PIFA with an all-textile metasurface for 5 GHz WBAN applications. *IEEE Antennas and Wireless Propagation Letters* **18**, 288–292.
- Yang H, Liu X, Fan Y and Xiong L (2022) Dual-band textile antenna with dual circular polarizations using polarization rotation AMC for off-body communications. *IEEE Transactions on Antennas and Propagation* **70**, 4189–4199.
- Annavarapu SK, Ghosh A, Singh LK, Chattopadhyay S and Sim C-Y-D (2022) Application of dielectric-artificial magnetic conductor composite substrate to design miniaturized P-band microstrip antenna for wireless underground sensor network. *IEEE Antennas and Wireless Propagation Letters* **21**, 2352–2356.
- Gupta S, Patil S, Dalela C and Kanaujia BK (2022) Circularly polarized fractal defected ground monopole antenna for Bluetooth/LTE/CNSS/S-band and CA-band applications. *Electromagnetics* **42**, 485–497.
- Yu C, Yang S, Chen Y and Zeng D (2019) Radiation enhancement for a tri-band microstrip antenna using an AMC reflector characterized with three zero-phases in reflection coefficient. *Journal of Electromagnetic Waves and Applications* **33**, 1846–1859.
- Gao M and Zhao X (2022) Design of tri-band patch antenna with enhanced bandwidth and diversity pattern for indoor wireless communication. *Applied Sciences* **12**, 7445.
- Jiang Z, Wang Z, Nie L, Zhao X and Huang S (2022) A low-profile ultra-wideband slotted dipole antenna based on artificial magnetic conductor. *IEEE Antennas and Wireless Propagation Letters* **21**, 671–675.
- Zhou C, Sun J, Yang -W-W, Li M and Wong H (2023) A wideband low-profile dual-polarized hybrid antenna using two different modes. *IEEE Antennas and Wireless Propagation Letters* **22**, 114–118.
- Lin B, Huang W, Guo J, Wang Y, Ye H and Ji X (2022) An ultra-wideband ellipse-shaped linear-to-circular polarization conversion metasurface with high efficiency. *Electromagnetics* **42**, 389–400.
- Singh V, Khalily M and Tafazolli R (2022) A metasurface-based electronically steerable compact antenna system with reconfigurable artificial magnetic conductor reflector elements. *iScience* **25**, 105549.
- El Atrash M, Abdalla MA and Elhennawy HM (2021) A compact highly efficient II-section CRLH antenna loaded with textile AMC for wireless body area network applications. *IEEE Transactions on Antennas and Propagation* **69**, 648–657.
- Saeed SM, Balanis CA, Birtcher CR, Durgun AC and Shaman HN (2017) Wearable flexible reconfigurable antenna integrated with artificial magnetic conductor. *IEEE Antennas and Wireless Propagation Letters* **16**, 2396–2399.
- Gong Y, Yang S, Li B, Chen Y, Tong F and Yu C (2020) Multi-band and high gain antenna using AMC ground characterized with four zero-phases of reflection coefficient. *IEEE Access* **8**, 171457–171468.
- Sievenpiper D, Zhang L, Broas RFJ, Alexopolous NG and Yablonoitch E (1999) High-impedance electromagnetic surfaces with a forbidden frequency band. *IEEE Transactions on Microwave Theory and Techniques* **47**, 2059–2074.
- Dewan R, Rahim MKA, Hamid MR, Yusoff MFM, Samsuri NA, Murad NA and Kamardin K (2017) Artificial magnetic conductor for various antenna applications: An overview. *International Journal of RF and Microwave Computer-Aided Engineering* **27**, e21105.
- Simovski CR, de Maagt P, Tretyakov SA, Paquay M and Sochava AA (2004) Angular stabilisation of resonant frequency of artificial magnetic conductors for TE-incidence. *Electronics Letters* **40**, 92.
- Smith DR, Vier DC, Koschny T and Soukoulis CM (2005) Electromagnetic parameter retrieval from inhomogeneous metamaterials. *Physical Review E* **71**, 036617.
- Nur LO, Kurniawan A, Sugihartono S and Munir A (2015) Theoretical analysis of resonant frequency for AMC-based absorber composed of square patch array. *International Journal on Electrical Engineering and Informatics* **7**, 284–296.



Rajavel V received his M.E. degree in Communication and Networking in 2017 from Madras Institute of Technology Campus, Anna University, Chennai. Currently, he is pursuing Ph.D. from National Institute of Technology Agartala. He has 3.5 years of academic experience. His research interests are antenna design and networking.



Dr. Dibyendu Ghoshal received a Ph.D. (Tech) degree from Calcutta University's Institute of Radio Physics and Electronics in 1997. He has more than 12 years of teaching experience. He is the author of more than 150 research articles. At the National Institute of Technology Agartala, he is an Associate Professor in the Electronics and Communication Engineering department. Microwave and millimeter wave technology and antenna engineering, digital signal and image processing with associated soft computing and optimization techniques, linear and nonlinear optics (along with photonics) and opto-electronics, semiconductor physics and devices, and digital signal processing are among his research and teaching interests.